

## MAGI1 as a link between endothelial activation and ER stress drives atherosclerosis

Jun-ichi Abe, ... , Scott E. Evans, Nhat-Tu Le

*JCI Insight*. 2019;4(7):e125570. <https://doi.org/10.1172/jci.insight.125570>.

Research Article

Cardiology

Cell biology

The possible association between the membrane-associated guanylate kinase with inverted domain structure-1 (MAGI1) and inflammation has been suggested, but the molecular mechanisms underlying this link, especially during atherogenesis, remain unclear. In endothelial cells (ECs) exposed to disturbed flow (d-flow), p90 ribosomal S6 kinase (p90RSK) bound to MAGI1, causing MAGI1-S741 phosphorylation and sentrin/SUMO-specific protease 2 T368 phosphorylation-mediated MAGI1-K931 deSUMOylation. MAGI1-S741 phosphorylation upregulated EC activation via activating Rap1. MAGI1-K931 deSUMOylation induced both nuclear translocation of p90RSK-MAGI1 and ATF-6-MAGI1 complexes, which accelerated EC activation and apoptosis, respectively. Microarray screening revealed key roles for MAGI1 in the endoplasmic reticulum (ER) stress response. In this context, MAGI1 associated with activating transcription factor 6 (ATF-6). MAGI1 expression was upregulated in ECs and macrophages found in atherosclerotic-prone regions of mouse aortas as well as in the colonic epithelia and ECs of patients with inflammatory bowel disease. Further, reduced MAGI1 expression in *Magi1*<sup>-/+</sup> mice inhibited d-flow-induced atherogenesis. In sum, EC activation and ER stress-mediated apoptosis are regulated in concert by two different types of MAGI1 posttranslational modifications, elucidating attractive drug targets for chronic inflammatory disease, particularly atherosclerosis.

Find the latest version:

<https://jci.me/125570/pdf>



# MAGI1 as a link between endothelial activation and ER stress drives atherosclerosis

Jun-ichi Abe,<sup>1</sup> Kyung Ae Ko,<sup>1</sup> Sivareddy Kotla,<sup>1</sup> Yin Wang,<sup>1</sup> Jesus Paez-Mayorga,<sup>2,3</sup> Ik Jae Shin,<sup>1</sup> Masaki Imanishi,<sup>1</sup> Hang Thi Vu,<sup>1</sup> Yunting Tao,<sup>2</sup> Miguel M. Leiva-Juarez,<sup>4</sup> Tamlyn N. Thomas,<sup>1</sup> Jan L. Medina,<sup>1</sup> Jong Hak Won,<sup>1</sup> Yuka Fujii,<sup>1</sup> Carolyn J. Giancursio,<sup>2</sup> Elena McBeath,<sup>1</sup> Ji-Hyun Shin,<sup>1</sup> Liliana Guzman,<sup>2</sup> Rei J. Abe,<sup>2</sup> Jack Taunton,<sup>5</sup> Naoki Mochizuki,<sup>6</sup> William Faubion,<sup>7</sup> John P. Cooke,<sup>2</sup> Keigi Fujiwara,<sup>1</sup> Scott E. Evans,<sup>4</sup> and Nhat-Tu Le<sup>2</sup>

<sup>1</sup>Department of Cardiology, The University of Texas MD Anderson Cancer Center, Houston, Texas, USA. <sup>2</sup>Center for Cardiovascular Regeneration, Department of Cardiovascular Sciences, Houston Methodist Research Institute, Houston Texas, USA. <sup>3</sup>Tecnologico de Monterrey, Escuela de Medicina y Ciencias de la Salud, Monterrey, Nuevo Leon, Mexico. <sup>4</sup>Department of Pulmonary Medicine, The University of Texas MD Anderson Cancer Center, Houston, Texas, USA. <sup>5</sup>Department of Cellular and Molecular Pharmacology, University of California, San Francisco, San Francisco, California, USA. <sup>6</sup>Department of Cell Biology, National Cardiovascular Center Research Institute, Osaka, Japan. <sup>7</sup>Division of Gastroenterology and Hepatology, Mayo Clinic, Rochester, Minnesota, USA.

The possible association between the membrane-associated guanylate kinase with inverted domain structure-1 (MAGI1) and inflammation has been suggested, but the molecular mechanisms underlying this link, especially during atherogenesis, remain unclear. In endothelial cells (ECs) exposed to disturbed flow (d-flow), p90 ribosomal S6 kinase (p90RSK) bound to MAGI1, causing MAGI1-S741 phosphorylation and sentrin/SUMO-specific protease 2 T368 phosphorylation-mediated MAGI1-K931 deSUMOylation. MAGI1-S741 phosphorylation upregulated EC activation via activating Rap1. MAGI1-K931 deSUMOylation induced both nuclear translocation of p90RSK-MAGI1 and ATF-6-MAGI1 complexes, which accelerated EC activation and apoptosis, respectively. Microarray screening revealed key roles for MAGI1 in the endoplasmic reticulum (ER) stress response. In this context, MAGI1 associated with activating transcription factor 6 (ATF-6). MAGI1 expression was upregulated in ECs and macrophages found in atherosclerotic-prone regions of mouse aortas as well as in the colonic epithelia and ECs of patients with inflammatory bowel disease. Further, reduced MAGI1 expression in *Magi1*<sup>-/-</sup> mice inhibited d-flow-induced atherogenesis. In sum, EC activation and ER stress-mediated apoptosis are regulated in concert by two different types of MAGI1 posttranslational modifications, elucidating attractive drug targets for chronic inflammatory disease, particularly atherosclerosis.

**Authorship note:** JA, KAK, SK, YW, JPM, and IJS contributed equally to this work. KF, SEE, and NTL are co-senior authors.

**Conflict of interest:** JT is a cofounder of Principia Biopharma, which has licensed the p90RSK inhibitor FMK-MEA.

**Copyright:** © 2019 American Society for Clinical Investigation

**Submitted:** October 16, 2018

**Accepted:** February 14, 2019

**Published:** April 4, 2019.

**Reference information:** *JCI Insight*. 2019;4(7):e125570. <https://doi.org/10.1172/jci.insight.125570>.

## Introduction

Inflammation is an important part of the innate defense system, but this system also plays negative roles in many cases of human diseases. For example, endothelial cell (EC) activation plays a key role in the pathogenesis of atherosclerosis. Proatherogenic agonists, such as inflammatory cytokines and growth factors as well as disturbed flow (d-flow), cause EC activation. In particular, d-flow, which is known to occur in so-called atheroprone areas of large arteries, activates proinflammatory and apoptotic signaling in ECs, leading to EC dysfunction (1, 2). A recent genome-wide association study of an independent cohort of patients with various diseases and healthy controls revealed a possible association between the membrane-associated guanylate kinase with inverted domain structure-1 (MAGI1) locus and the severity of several chronic inflammatory diseases, such as inflammatory bowel disease (IBD), psoriasis, and neuroticism (3–6). Concordantly, MAGI1 mRNA expression levels in small intestine mucosa are increased in patients with IBD (3). These observations suggest that MAGI1 may be involved in the mechanism of EC activation.

MAGI1 is a scaffold protein that contains 6 PSD95/DiscLarge/ZO-1 (PDZ) domains, a guanylate kinase domain, and 2 WW (rsp5) domains flanked by the first and second PDZ domains. MAGI1 is widely

expressed across tissues with the exception of skeletal muscle (7). MAGI1 associates with the tight and adherens junctions (8, 9). Depletion of MAGI1 suppresses cell-cell contact–induced activation of Rap1, a member of the Ras-like small GTPase family. Rap1 activation, in turn, causes vinculin relocation to focal adhesions and VE-cadherin/ $\beta$ -catenin complexes. Thus, MAGI1 is crucial for VE-cadherin–mediated adherens junction maturation and cell-cell adhesion (9). MAGI1 can also associate with a variety of molecules via its PDZ domains, such as phosphatase and tensin homolog deleted on chromosome 10, RapGEF2, and thyroid receptor-interacting protein-6 (8–10), and plays a tumor-suppressive role by stabilizing tight junctions.

p90 ribosomal S6 kinase (p90RSK) is a ubiquitously expressed ([https://www.nextprot.org/entry/NX\\_Q15418/expression](https://www.nextprot.org/entry/NX_Q15418/expression)) serine/threonine kinase that functions downstream from the Raf/mitogen-activated protein kinase kinase/ERK1/2 signaling pathway (11). However, we have also reported that p90RSK activation may occur independently of the ERK1/2 pathway (12). Activation and nuclear translocation of p90RSK occur concomitantly with immediate early expression of genes, such as c-fos and Egr-1 (13, 14). p90RSK is also involved in NF- $\kappa$ B activation by phosphorylating I $\kappa$ B $\alpha$  and transcription factors c-Fos, Nur77, and CREB (15). Although ERK5 can be an upstream kinase that regulates p90RSK activity, as it does with ERK1/2 (16), we found that p90RSK directly phosphorylates ERK5-S496 and inhibits its transcriptional activity, resulting in EC activation and vascular reactivity (17). Furthermore, we demonstrated a crucial role for p90RSK as a downregulator of the deSUMOylation function of sentrin/SUMO-specific protease 2 (SEN2) for p53 and ERK5 by promoting SEN2 nuclear export (18). We showed that d-flow activates p90RSK and phosphorylates SEN2-T368 in the nucleus. Phosphorylated SEN2 is exported from the nucleus, increasing SUMOylation of nuclear proteins, including p53 and ERK5, that result in EC activation and apoptosis (18).

The purpose of the present study was to determine the role of MAGI1 in the severity of chronic inflammatory diseases. We hypothesized that MAGI1 posttranslational modifications (PTMs) enhance inflammatory responses. We report herein that p90RSK associates with MAGI1 in ECs and executes 2 independently regulated PTMs of MAGI1: S741 phosphorylation and K931 deSUMOylation. MAGI1-S741 phosphorylation is vital for Rap1 activation. MAGI1-K931 deSUMOylation, on the other hand, is required for nuclear p90RSK translocation, as non-SUMOylated MAGI1 translocates to the nucleus and carries p90RSK with it. In the nucleus, p90RSK phosphorylates ERK5-S496 and SEN2-T368, consequently increasing cellular inflammation (17, 19, 20). We observed that depletion of MAGI1 significantly inhibited d-flow–induced atherogenesis. Furthermore, our transcriptome analysis demonstrated downregulation of endoplasmic reticulum (ER) stress–related gene expression in ECs via reduction of *Magi1* expression, which plays a crucial role in regulating p90RSK-mediated EC apoptosis. This is the first study to our knowledge that demonstrates the key role of the p90RSK-MAGI1 signaling module in the context of EC activation and apoptosis. Our results suggest that MAGI1 simultaneously regulates EC activation and ER stress–induced apoptosis, which are critical molecular events for atherogenesis, via MAGI1-S741 phosphorylation and MAGI1-K931 SUMOylation.

## Results

*MAGI1* expression is required for d-flow–induced EC activation. Lexicon Pharmaceuticals generated *Magi1*-knockout (*Magi1*<sup>−/−</sup>) mice via gene-trap insertion (*Magi1*<sup>Gt(OST33326)Lox</sup>). We confirmed the depletion of *Magi1* in these mice by IB tissue lysates obtained from *Magi1*<sup>−/−</sup> and nontransgenic littermate control (NLC) mice with an anti-MAGI1 antibody (Figure 1A, middle). Body size and weight, development, life span, and organ structures at the gross anatomic level in the NLC and *Magi1*<sup>+/-</sup> mice were indistinguishable (Supplemental Figure 1A; supplemental material available online with this article; <https://doi.org/10.1172/jci.insight.125570DS1>). First, to determine the role of MAGI1 in regulation of EC activation, we isolated mouse lung ECs (MLECs) from NLC and *Magi1*<sup>−/−</sup> animals and exposed them to 2 inflammatory conditions: stimulation by TNF- $\alpha$  and overexpression of p90RSK. These conditions are known to activate NF- $\kappa$ B, a prototypical proinflammatory molecule, and to increase VCAM-1 expression in ECs (2, 21). Treatment with TNF- $\alpha$  increased VCAM-1 expression in NLC MLECs but not in *Magi1*<sup>−/−</sup> MLECs (Figure 1A, top, and Figure 1B). The NF- $\kappa$ B activation induced by TNF- $\alpha$  stimulation and p90RSK overexpression in NLC MLECs was abolished in *Magi1*<sup>−/−</sup> MLECs (Figure 1C). Similarly, depletion of MAGI1 in human umbilical vein ECs (HUVECs; Figure 1, D and E) and human colonic epithelial cells (Figure 1F) by treatment with siRNA markedly inhibited NF- $\kappa$ B activation by d-flow, TNF- $\alpha$ , and thrombin (Thb) (Figure 1, E and F) as well as expression of VCAM-1, ICAM-1, and E selectin induced by d-flow (Figure 1G and Supplemental Figure 1, B and C).

Next, we investigated whether reduced MAG11 expression affected the inflammatory state of ECs in vivo by measuring the expression level of inflammatory marker VCAM-1. We coimmunostained en face preparations of aortas obtained from NLC and *Magi1*<sup>+/-</sup> mice with anti-VCAM-1 and -VE-cadherin, using the latter to mark ECs. For confocal imaging, we focused on 2 areas of the aortic arch: the lesser curvature, where ECs are exposed to d-flow, and the greater curvature, where ECs are exposed to laminar blood flow (l-flow) (15, 22). Because these two areas are separated by a small distance (<1 mm), any difference in their intensity of staining is unlikely to be due to technical factors. We found that the intensity of anti-VCAM-1 staining was low in the l-flow area but high in the d-flow area in NLC mice as we reported previously (19). In contrast, the intensity of anti-VCAM-1 staining was markedly decreased in both l-flow and d-flow areas in *Magi1*<sup>+/-</sup> mice (Figure 1H). Taken together, these results suggest that MAG11 plays a critical role in regulation of inflammation, especially in ECs.

Since blood pressure (BP) can change the EC phenotype indirectly, we measured BP of control and *Magi1*<sup>+/-</sup> mice. Both groups were normotensive, eliminating a possible effect of BP on *Magi1*<sup>+/-</sup> EC phenotype (Supplemental Figure 2A). Furthermore, we found no difference in plasma IL-6 levels (Supplemental Figure 2B) and circulating levels of various hematopoietic cells (Supplemental Table 1) between *Magi1*<sup>+/-</sup> and control mice. Additionally, we explored the inflammatory response of peripheral blood mononuclear cells (PBMCs), bone marrow-derived macrophages (BMDMs), splenocytes, and vascular smooth muscle cells (VSMCs) isolated from *Magi1*<sup>+/-</sup> and control mice. Increased IL-1 $\beta$  levels upon stimulation with TNF- $\alpha$  were the same between *Magi1*<sup>+/-</sup> and control cells (Supplemental Figure 2C). These data suggest that, in the context of atherosclerosis, the contribution of MAG11 to inflammation is unique to ECs rather than other atherosclerosis-related cell types.

*p90RSK associates with MAG11 and upregulates EC activation.* p90RSK and MAG11 association has been suggested (23), but the physiological role of this interaction is unknown. Therefore, we investigated whether MAG11 plays a role in d-flow-induced p90RSK activation and found that, in *Magi1*<sup>-/-</sup> MLECs, d-flow-induced p90RSK activation was unaffected (Supplemental Figure 3A), indicating that MAG11 is not an upstream regulator of p90RSK activation. Next, we examined the extent of MAG11-p90RSK interaction under inflammatory conditions by coimmunoprecipitation and found that the association of p90RSK with MAG11 was enhanced in ECs treated with d-flow or Thb (Figure 2, A and B). The region of MAG11 containing its WW2 and PDZ2 domains (amino acids 362–543) is suggested to be a p90RSK-binding site (23). Thus, we transfected ECs with an adenoviral construct encoding for this region (an inhibitory fragment with WW2 and PDZ2 domains [IFWP]) or a control vector together with Flag-tagged WT p90RSK and MAG11-WT. Next, we performed co-IP experiments using an anti-MAG11 antibody and found that overexpression of Flag-tagged p90RSK was coimmunoprecipitated with MAG11 (Figure 2C). In cells transfected with the IFWP construct, the interaction of p90RSK with MAG11 was inhibited in a dose-dependent manner (Figure 2, D and E, and Supplemental Figure 3, B and C). More importantly, IFWP inhibited d-flow-, Thb-, and TNF- $\alpha$ -induced NF- $\kappa$ B activation as well as adhesion molecule expression (Figure 2, F and G). These results establish for the first time to our knowledge the crucial role of the association of p90RSK with MAG11 in regulation of EC activation.

*MAG11-S741 phosphorylation by p90RSK leads to Rap1 activation and EC activation.* To elucidate the mechanisms by which p90RSK activation regulates MAG11 function, we analyzed the MAG11 amino acid sequence for possible phosphorylation site(s) catalyzed by p90RSK. Using publicly available data sets for system-wide characterization of parallel quantitative proteomic and phosphoproteomic analyses (neXtProt; [http://www.nextprot.org/db/entry/NX\\_Q96QZ7/proteomics](http://www.nextprot.org/db/entry/NX_Q96QZ7/proteomics)) and the Group-based Prediction System software program (version 2.0) (24), we found 2 possible sites: S741 and S748. D-flow- and p90RSK overexpression-induced NF- $\kappa$ B activation observed in ECs transfected with MAG11-WT was abolished in ECs expressing MAG11-S741A but not in those expressing MAG11-S748A (Figure 3A and Supplemental Figure 3D). To confirm that MAG11-S741 is actually phosphorylated by p90RSK, we generated affinity-purified rabbit antibodies against MAG11 with phosphorylated S741 and designed adenoviral vectors to overexpress Flag-MAG11-WT or Flag-MAG11-S741A in ECs (Ad-Flag-MAG11-WT and Ad-Flag-MAG11-S741A, respectively). Upon d-flow stimulation, MAG11 was phosphorylated in cells overexpressing Ad-Flag-MAG11-WT but not Ad-Flag-MAG11-S741A, demonstrating the specificity of our antibody (Figure 3B). D-flow-induced S741 phosphorylation was downregulated in ECs expressing dominant-negative (DN; i.e., kinase-dead) p90RSK, indicating a functional role for p90RSK activation in MAG11-S741 phosphorylation (Figure 3C). Furthermore, an in vitro kinase assay using

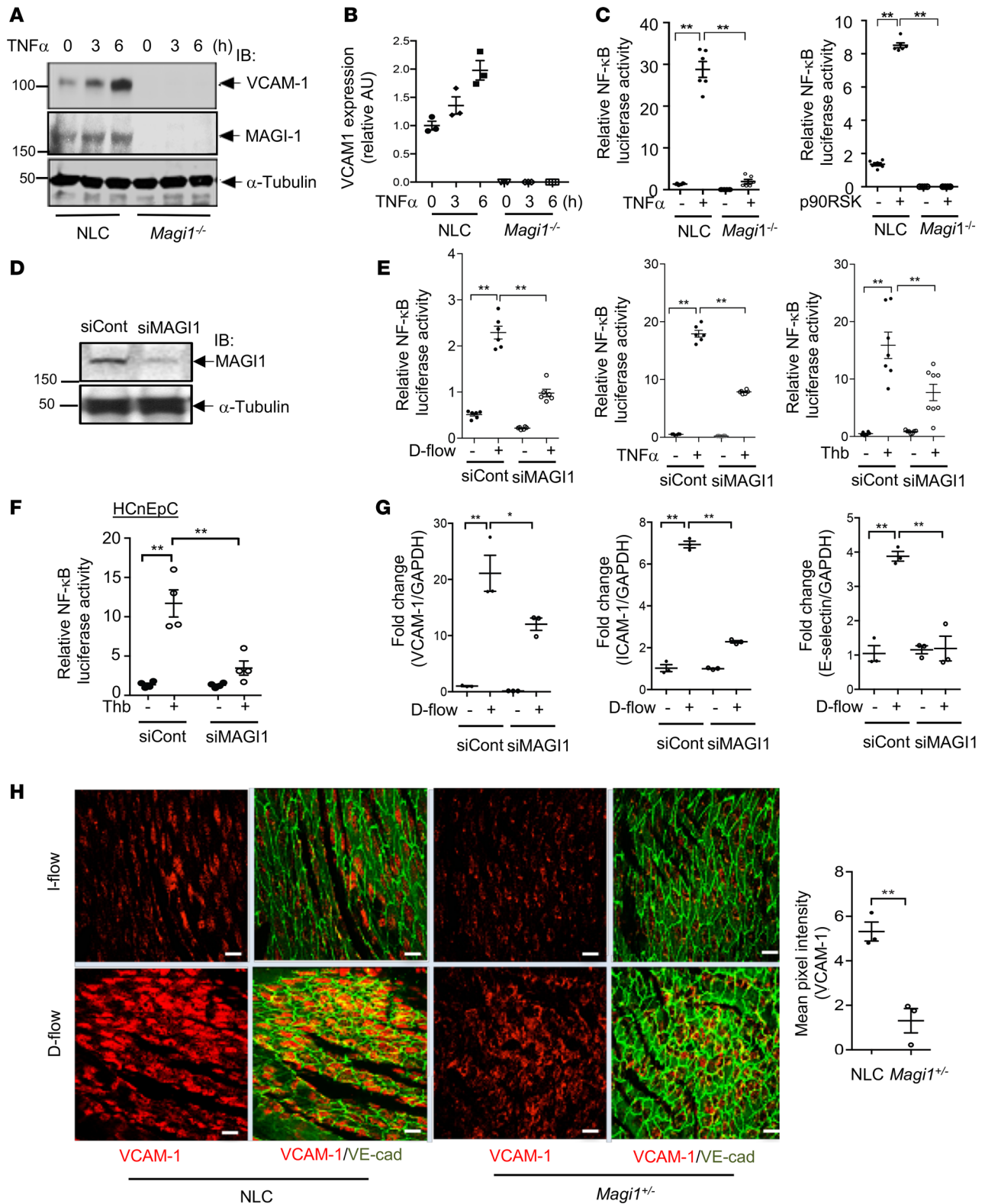


**Figure 1. MAGI1 expression is required for d-flow-induced EC activation.** (A and B) Expression of VCAM-1, MAGI1, and  $\alpha$ -tubulin in NLC and *Magi1*<sup>-/-</sup> MECs treated with TNF- $\alpha$  (10 ng/ml) for 0–6 hours was determined by Western blotting. (B) VCAM-1 expression quantified by densitometry. Data represent mean  $\pm$  SEM ( $n = 3$ ).  $P < 0.0001$  between NLC and *Magi1*<sup>-/-</sup> groups. (C) MAGI1 depletion inhibits NF- $\kappa$ B activation. MECs were subjected to an NF- $\kappa$ B activity assay in the presence (right) or absence (left) of p90RSK overexpression. Cells were then treated with TNF- $\alpha$  for 24 hours (10 ng/ml, left), and their NF- $\kappa$ B activity was measured. Data represent mean  $\pm$  SEM ( $n = 6$ ).  $**P < 0.01$ . (D) MAGI1 expression is reduced in HUVECs treated with siRNA-targeted *Magi1* (siMAGI1). siCont, control siRNA. (E) MAGI1 depletion inhibits NF- $\kappa$ B activation. HUVECs were transfected with the indicated siRNAs and then treated with or without d-flow (left), TNF- $\alpha$  (10 ng/ml, middle), or Thb (10 U/ml, right) for 24 hours, and their relative NF- $\kappa$ B luciferase activity was measured. Data represent mean  $\pm$  SEM ( $n = 6$ ).  $**P < 0.01$ . (F) MAGI1 depletion inhibits NF- $\kappa$ B activation in human colonic epithelial cells (HCnEpC). Cells were transfected

with the indicated siRNAs and treated with or without Thb (10 U/ml for 24 hours), and their relative level of NF- $\kappa$ B luciferase activity was measured. Data represent mean  $\pm$  SEM ( $n = 6$ ). **(G)** MAGI1 depletion inhibits d-flow-induced expression of adhesion molecules. siRNA-treated ECs were exposed to d-flow, total RNA was obtained from the cells, and levels of VCAM-1, ICAM-1, and E selectin RNA expression were quantified using qRT-PCR. Data represent mean  $\pm$  SEM ( $n = 3$ ). \* $P < 0.05$ ; \*\* $P < 0.01$ . **(H)** Reduced intensity of VCAM-1 staining in the d-flow region in the *Magi1*<sup>-/-</sup> mouse group. En face preparations of mouse aortas were coimmunostained with anti-VE-cadherin and -VCAM-1 antibodies. Fluorescent images of anti-VCAM-1 staining in aorta areas exposed to l-flow and d-flow were recorded using confocal laser scanning microscopy (left). Scale bars: 20  $\mu$ m. Data represent mean  $\pm$  SEM ( $n = 3$ ). \*\* $P < 0.01$ . Statistical differences between 2 independent groups **(H)** were assessed using the 2-tailed Student's *t* test and 1-way ANOVA followed by Bonferroni's post hoc testing for multiple groups **(B, C, E, F, and G)**.

recombinant p90RSK and immunoprecipitated MAGI1 showed that p90RSK can directly phosphorylate MAGI1 S741 (Figure 3D). Finally, expression of both d-flow- and Thb-induced VCAM-1, ICAM-1, and E selectin was markedly lower in MAGI1-S741A-transfected ECs than in MAGI1-WT-transfected ECs (Figure 3, E–G). Taken together, p90RSK can directly phosphorylate MAGI1 S741, which is required for upregulation of EC activation.

A previous study reported the role of MAGI1 in regulation of Rap1 activity (9). We applied d-flow to ECs transfected with a DN form of Rap1 (Rap1-N17) along with an NF- $\kappa$ B reporter gene and found that NF- $\kappa$ B activation was inhibited (Figure 4A). In addition, Rap1 activation was completely inhibited by transduction with adenoviral vectors containing DN (kinase-dead) p90RSK (Ad-DN-p90RSK) and MAGI1-S741A (Ad-MAGI1-S741A) (Figure 4, B–D). These results demonstrate a vital role for MAGI1-S741 phosphorylation in regulating Rap1 activation and subsequent EC activation.

*D-flow and Thb induce MAGI1 deSUMOylation via p90RSK activation and accelerate EC activation.* SUMOylation is a PTM akin to ubiquitination by which small ubiquitin-like proteins called SUMOs are enzymatically conjugated to target proteins (25). We found that MAGI1 was constitutively SUMOylated in ECs and deSUMOylated by treatment with d-flow and Thb (Figure 5A and Supplemental Figure 3E). This deSUMOylation was significantly inhibited by a highly selective inhibitor of p90RSK, fluoromethyl ketone-methoxyethylamine (FMK-MEA) (Figure 5, A and B), and by transduction of Ad-DN-p90RSK (Supplemental Figure 3E). FMK-MEA inhibited p90RSK but not c-Jun N-terminal kinase, ERK1/2, or p38 activity (Supplemental Figure 3F), further demonstrating that FMK-MEA is a highly selective inhibitor of p90RSK (17). SENP2 is a deSUMOylation enzyme localized predominantly in the nucleus, but with the ability to shuttle between the nucleus and cytoplasm (26). We previously reported that activated p90RSK phosphorylates SENP2 at T368, facilitating nuclear SENP2 export (27). As a consequence, the reduction of functional SENP2 in the nucleus leads to increased SUMOylation of nuclear proteins, such as ERK5 and p53 (18). To determine whether MAGI1 deSUMOylation in ECs by inflammatory stimuli results from the nuclear export of SENP2, we induced overexpression of SENP2-T368A mutant, which cannot translocate to the cytoplasm (18). Transduction of ECs with Ad-SENP2-T368A markedly inhibited d-flow-induced MAGI1 deSUMOylation (Figure 5, C and D). Of note, because WT SENP2 resides mainly in the nucleus, its overexpression does not alter basal MAGI1 SUMOylation, which is localized in the extranuclear compartment. However, upon d-flow stimulation, WT SENP2 translocates to the cytoplasm and deSUMOylates MAGI1. In contrast, because SENP2 T368A mutant is confined to the nucleus, MAGI1 is not deSUMOylated under d-flow (18). These results demonstrate a crucial role for nuclear export of SENP2 in MAGI1 deSUMOylation.

Using the SUMOsp 2.0 prediction software program, we identified MAGI1-K931 as a possible SUMOylation site (28). In the present study, we found that the MAGI1 SUMOylation level was markedly lower in MAGI1-K931R-transfected ECs than in MAGI1-WT-transfected ECs (Figure 5E). To account for possible nonspecific binding of antibodies to SUMO, we induced overexpression of histidine-tagged (His-tagged) SUMO3 with Flag-tagged SUMOylatable MAGI1-WT or a non-SUMOylatable MAGI1-K931R mutant and used nickel-nitrotri-acetic acid resin to pull down His-tagged SUMO3. We observed that MAGI1 was pulled down from the lysate of cells overexpressing MAGI1-WT but not MAGI1-K931R (Figure 5, F and G). We also induced overexpression of Myc-SUMO3 with Flag-tagged MAGI1-WT in ECs and detected MAGI1 SUMOylation in this setting (Supplemental Figure 4A, left). Finally, we determined that endogenous MAGI1 was SUMOylated using two different antibodies (rabbit in Figure 5A and mouse anti-MAGI1 in Figure 5C and Supplemental Figure 4A, right) and confirmed that d-flow significantly inhibited MAGI1 SUMOylation. Based on the results obtained using 4 different approaches, we conclude with fair certainty that MAGI1 is SUMOylated in ECs. Furthermore, we found that TNF- $\alpha$ - and d-flow-induced NF- $\kappa$ B activation and adhesion molecule expression were enhanced in ECs transfected with the MAGI1-K931R mutant (Figure 5, H–J). Taken together, these results suggest an inhibitory effect

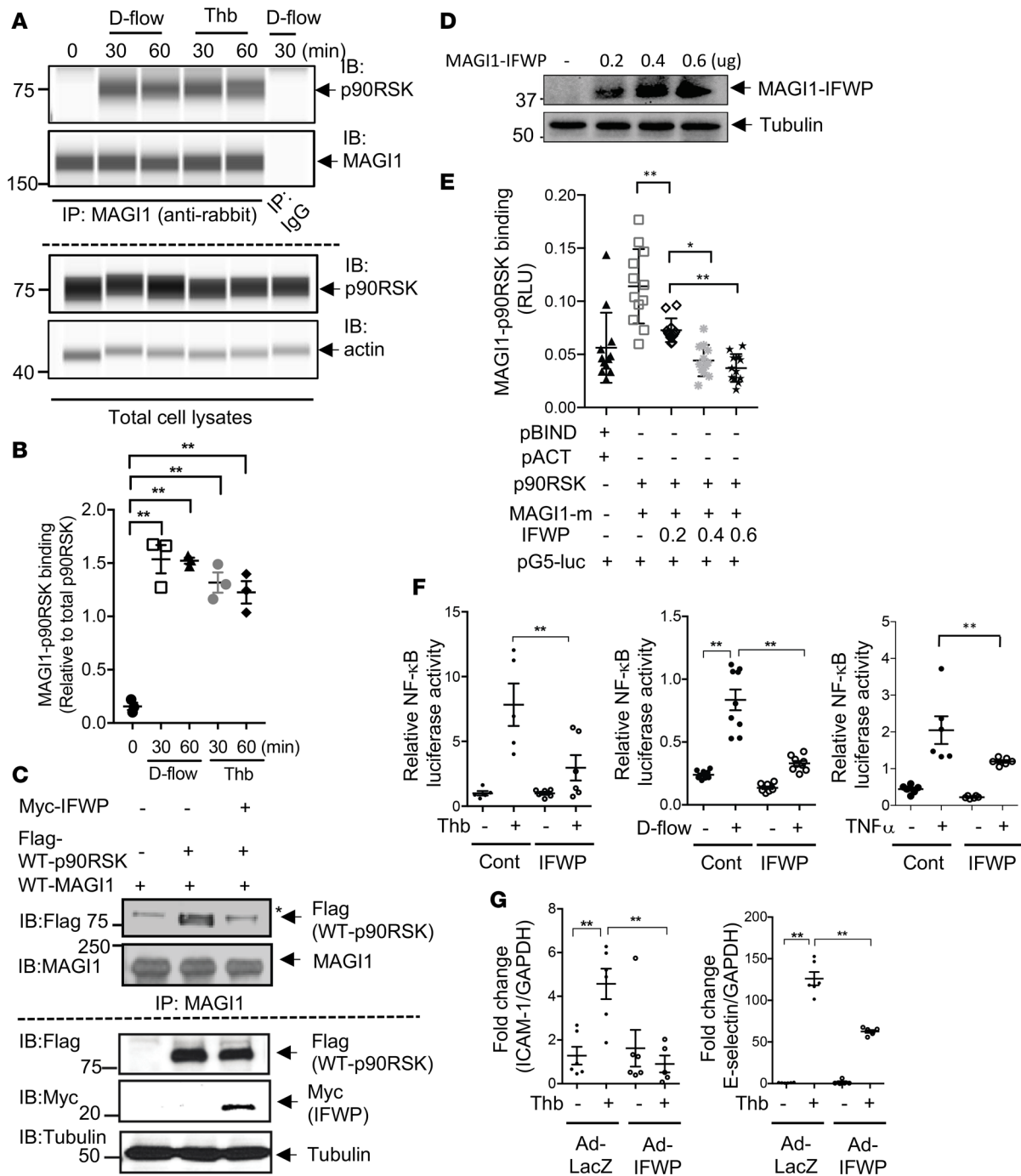


**Figure 2. MAG1-p90RSK association promotes EC activation.** (A and B) p90RSK associates with MAG1. HUVECs were exposed to d-flow or treated with Thb (10 U/ml (A and B), and their MAG1-p90RSK interaction was assessed via co-IP with an anti-MAG1 antibody followed by IB with an anti-p90RSK antibody (top row) and then with an anti-MAG1 antibody (second row) to confirm pull-down of equal amounts of MAG1 protein. The rows below the dotted line show the p90RSK and actin levels in the cell lysates. Simple Western blotting with Wes system (Proteinsimple) was used. A rabbit IgG was used as a negative control. Quantification of the ratio of coimmunoprecipitated p90RSK and MAG1 after treatment with d-flow and Thb (B) and the fold increase in ECs from the mean value at 0 minutes. Data represent mean ± SEM (n = 3). (C) MAG1-p90RSK interaction and pulled down MAG1 (above the dotted line) and expression of p90RSK, IFWP (amino acid 362–543 fragment), and tubulin (below the dotted line) in HeLa cells expressing Flag-tagged p90RSK and MAG1-WT in the presence or absence of Myc-tagged IFWP as in A were assessed. The asterisk indicates nonspecific bands. Representative blots from 3 independent experiments are shown. (D and E) MAG1-p90RSK binding detected using a CheckMate Mammalian Two-Hybrid Assay was dose-dependently inhibited in cells expressing IFWP. The dose-dependent expression of IFWP was confirmed via Western blotting using anti-Myc (IFWP) and anti-tubulin antibodies (D). The Data represent mean ± SEM (n = 6–12). (F and G) p90RSK-MAG1 binding increases NF-κB activity and adhesion molecule expression. (F) Bovine aortic ECs (left) and HUVECs (middle and right) expressing IFWP were subjected to an NF-κB activity assay under Thb (10 U/ml left) or TNF-α (10 ng/ml right) stimulation for 12 hours or d-flow stimulation for 24 hours. The relative NF-κB activity in the cells was measured. Data represent mean ± SEM (n = 5–9). (G) HUVECs transduced with Ad-LacZ or -IFWP (multiplicity of infection [MOI], 20) were treated with Thb (10 U/ml, 24 h), and expression of ICAM-1 and E selectin RNA was quantified. Data represent mean ± SEM (n = 5–6). \*\*P < 0.01. Statistical differences were assessed using the 1-way ANOVA followed by Bonferroni's post hoc testing for multiple groups.

of MAGI1 SUMOylation on EC activation.

To study the possible interplay between MAGI1 phosphorylation and deSUMOylation in ECs, we transduced ECs with Ad-MAGI1-K931R or -MAGI1-S741A mutants and examined the ensuing d-flow-induced MAGI1-S741 phosphorylation and MAGI1-K931 deSUMOylation. We found that overexpression of the MAGI1-K931R mutant did not affect MAGI1 phosphorylation and that MAGI1 deSUMOylation was not influenced by MAGI1-S741A mutant expression (Supplemental Figure 4, B–E). These data suggest that d-flow independently induces these 2 PTMs.

*DeSUMOylation of MAGI1 elicits nuclear translocation of both MAGI1 and p90RSK.* MAGI1 deSUMOylation depends on nuclear export of SENP2, which is regulated by SENP2-T368 phosphorylation (Figure 5, C and D). In unstimulated ECs, MAGI1 is found in the cytoplasm and along the plasma membrane (Figure 6A, white arrows), but a considerable level of nuclear localization was observed in cells stimulated by Thb (Figure 6A, yellow arrows; Figure 6B; and Supplemental Figure 5). Upon transduction of ECs with Ad-Flag-MAGI1-K931R, this SUMOylation-defective MAGI1 mutant was localized exclusively in the nucleus, even in the absence of inflammatory stimulation (Figure 6, B–D, and Supplemental Figure 5).

Given the importance of the p90RSK interaction with MAGI1 in the regulation of d-flow-induced EC activation (Figure 2), we investigated the localization of endogenous p90RSK in ECs transduced with Ad-Flag-MAGI1-K931R or Ad-LacZ (control) via immunostaining. We found that p90RSK was generally excluded from the nuclei in control ECs but localized in the nuclei in MAGI1-K931R-transduced ECs (Figure 6, C–F). To determine whether MAGI1 regulates nuclear translocation of p90RSK, we treated ECs with MAGI1 siRNA, transduced them with Ad-Flag-p90RSK, and treated them with Thb. p90RSK and MAGI1 translocated from the cytosol to the nucleus after 30–60 minutes of Thb treatment (Figure 6, C–F). However, MAGI1 depletion inhibited nuclear translocation of p90RSK (Figure 6, E and F). These results suggest a role for MAGI1, especially its deSUMOylated form, in nuclear translocation of p90RSK. To determine the role of MAGI1 deSUMOylation in the regulation of p90RSK-mediated nuclear events, we investigated whether MAGI1 and its states of SUMOylation affected p90RSK-ERK5 binding, as we previously showed that nuclear p90RSK-ERK5 association causes EC activation (17). Using a mammalian 2-hybrid assay, we found that p90RSK-ERK5 binding was greatly enhanced by overexpression of the deSUMOylated form of MAGI1 (MAGI1-K931R mutant) (Figure 6G). These results suggest that MAGI1 regulates nuclear p90RSK-mediated EC activation.

*The role of MAGI1 in d-flow-induced atherosclerotic plaque formation and of increased MAGI1 expression in tissue samples from patients with chronic inflammatory diseases.* Our in vitro data demonstrate that MAGI1 plays an essential role in EC activation. To determine whether MAGI1 is involved in d-flow-induced atherosclerotic plaque formation, we used a left carotid artery (LCA) partial ligation mouse model in which all of the branching arteries of the LCA, except for the occipital artery, were ligated to create d-flow within the LCA. We generated this model using atheroprone mice with knockdown of LDL receptor expression (*Ldlr*<sup>-/-</sup> mice) crossed with *Magi*<sup>+/-</sup> mice, yielding *NLC/Ldlr*<sup>-/-</sup> and *Magi*<sup>+/-</sup>/*Ldlr*<sup>-/-</sup> mice (29–31). We observed no notable differences in body weight, fasting glucose, HDL, or LDL levels between the *NLC/Ldlr*<sup>-/-</sup> and *Magi*<sup>+/-</sup>/*Ldlr*<sup>-/-</sup> mice after partial ligation of the LCA (Supplemental Figure 1A and Supplemental Figure 6A). Four weeks after ligation, intimal thickening (i.e., neointima formation) observed in *NLC/Ldlr*<sup>-/-</sup> mice was inhibited in *Magi*<sup>+/-</sup>/*Ldlr*<sup>-/-</sup> mice (Figure 7, A and B). We found accumulation of macrophages stained with Mac3 in the neointima of *NLC/Ldlr*<sup>-/-</sup> mice, a hallmark of vascular inflammation and atherosclerosis. However, macrophage infiltration was downregulated in *Magi*<sup>+/-</sup>/*Ldlr*<sup>-/-</sup> mice (Supplemental Figure 6B). These results demonstrate a critical role for MAGI1 in d-flow-induced atherogenesis. Furthermore, we performed double staining for MAGI1 and Mac3 and found colocalization of anti-MAGI1 and anti-Mac3 staining (Pearson correlation coefficient,  $0.68850 \pm 0.02285$ , mean  $\pm$  SEM) in atherosclerotic lesions of the LCA after partial carotid ligation (PCL) (Supplemental Figure 7, A–D). We also found that anti-MAGI1 staining in the EC layer of the LCA after PCL was much stronger than that in control nonatherosclerotic RCA (Supplemental Figure 7, A–E). In contrast, we did not observe a significant increase in the intensity of MAGI1 staining of the medial layer of the LCA after PCL (Supplemental Figure 7F). Taken together, these data suggest that MAGI1 expression is upregulated in macrophages and ECs in atherosclerotic lesions. We also performed PCL in *NLC/Ldlr*<sup>-/-</sup> and *Magi*<sup>+/-</sup>/*Ldlr*<sup>-/-</sup> mice but did not detect any additive effects of complete MAGI1 depletion on the d-flow-induced plaque formation (Supplemental Figure 7G).

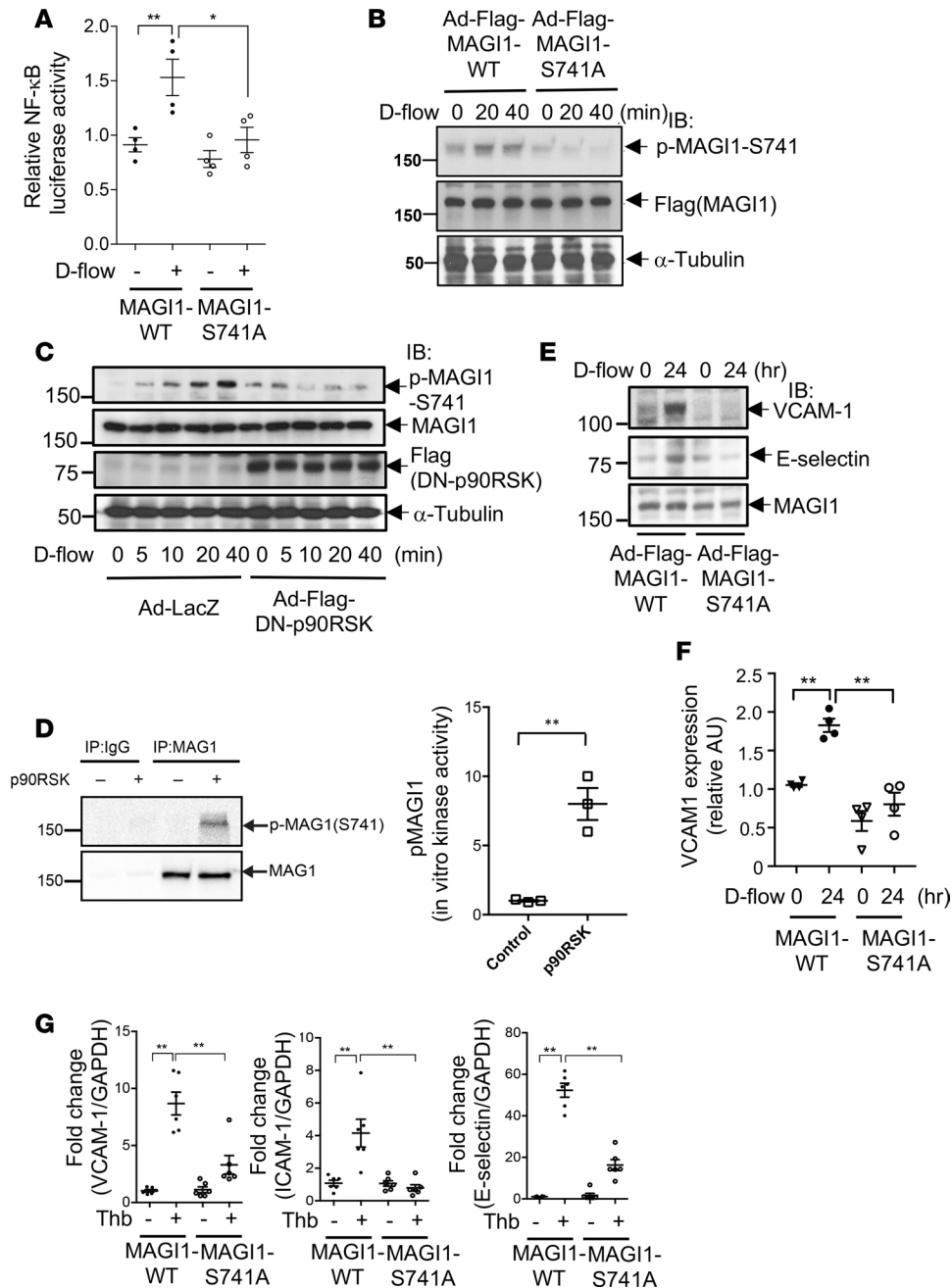


**Figure 3. A role for MAGI1-S741 phosphorylation in EC activation.** (A) D-flow–induced NF- $\kappa$ B activation is reduced in HUVECs expressing the MAGI1-S741A mutant. ECs expressing MAGI1-WT or -S741A were subjected to an NF- $\kappa$ B activity assay with exposure to d-flow for 24 hours, and the relative NF- $\kappa$ B luciferase activity in the cells was measured. Data represent mean  $\pm$  SEM ( $n = 4$ ).  $*P < 0.05$ ;  $**P < 0.01$ . (B–F) p90RSK phosphorylates MAGI1-S741 and mediates expression of adhesion molecules. ECs transduced (MOI, 20) with Ad-Flag MAGI1-WT or -S741A (B, E–G), and Ad-LacZ or Flag DN-p90RSK (C) were exposed to d-flow (B, C, E, and F) or Thb (10 U/ml, 24 h) (G), and phosphorylation of MAGI1-S741 (B and C) and expression of MAGI1, DN-p90RSK, VCAM-1, E selectin, and tubulin (B, C, E, and F) were assayed using IB. (D) In vitro phosphorylation of MAGI1 by p90RSK was performed, and MAGI1 was immunoprecipitated and immunoblotted with anti-phospho-MAGI1 (S741) (top). The same amount of MAGI1 was immunoprecipitated by anti-MAGI1, but not by non-immune IgG (bottom). The graph shows densitometric quantification of phosphorylated MAGI1-S741, which was normalized by total MAGI1 protein levels. Data represent mean  $\pm$  SEM ( $n = 3$ ).  $**P < 0.01$ . (F) Densitometric data for immunoblots of VCAM-1 ( $n = 4$ ), which were similar to those shown in E. Data represent mean  $\pm$  SEM.  $**P < 0.01$ . (G) Levels of VCAM-1, ICAM-1, and E selectin RNA expression were quantified. Data represent mean  $\pm$  SEM ( $n = 4–6$ ).  $**P < 0.01$ . Statistical differences between 2 independent groups (D) were assessed using the 2-tailed Student's  $t$  test and 1-way ANOVA followed by Bonferroni's post hoc testing for multiple groups (A, F, and G).

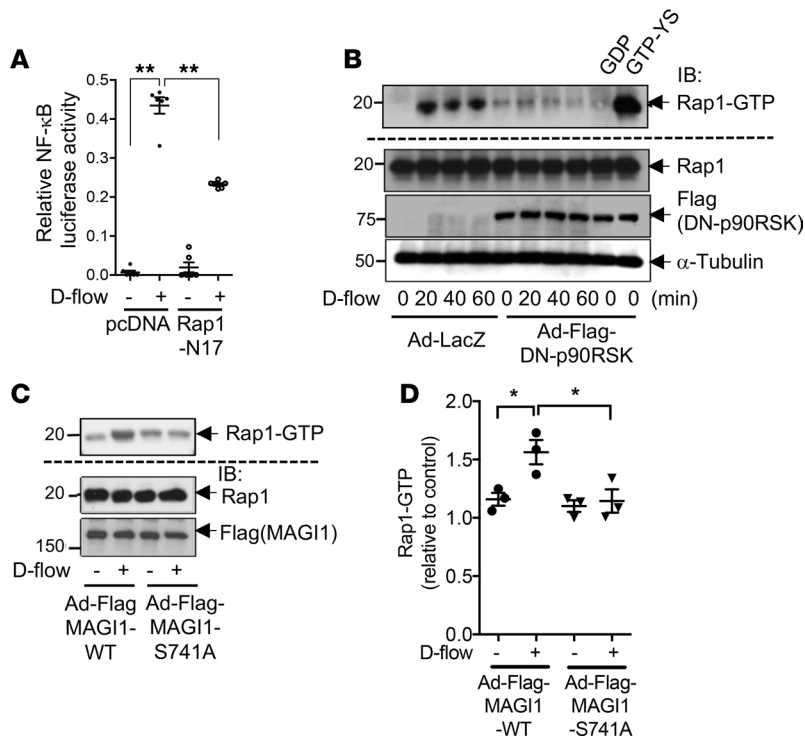


**Figure 4. The role of p90RSK-mediated MAGI1-S741 phosphorylation in regulating Rap1 activation.** (A) Activation of the small GTPase Rap1 in d-flow-induced NF- $\kappa$ B activation. HUVECs expressing a DN form of Rap1 (Rap1-N17) were subjected to an NF- $\kappa$ B activity assay with d-flow stimulation (24 h), and the relative NF- $\kappa$ B luciferase activity in the cells was measured. Data represent mean  $\pm$  SEM ( $n = 6$ ).  $**P < 0.01$ . (B–D) p90RSK activation and MAGI1-S741 phosphorylation in ECs with d-flow-induced Rap1 activation. ECs transduced with Ad-LacZ or Ad-Flag-DN-p90RSK (B) or Ad-Flag-MAGI1-WT or Ad-Flag-MAGI1-S741A (C) (MOI, 20) were exposed to d-flow for the indicated times (B) or 20 minutes (C). The level of Rap1-GTP expression in ECs was measured using Rap1 pull-down assays (above the dotted line). The levels of total Rap1, DN-p90RSK, MAGI1, and tubulin expression were determined using IB (B, below the dotted line). Shown are representative blots from 3 independent experiments. (D) The Rap1-GTP expression level in C was quantified ( $n = 3$ ). Data represent mean  $\pm$  SEM.  $*P < 0.01$ . Statistical differences were assessed using 1-way ANOVA followed by Bonferroni's post hoc testing for multiple groups.

Next, we examined whether the level of MAGI1 expression correlates with blood flow patterns within the aortic arch. To that end, we coimmunostained en face preparations of aortas from control *Magi1*<sup>+/+</sup> mice fed normal chow (NC) with anti-MAGI1 and anti-VE-cadherin. We found considerably higher levels of MAGI1 expression in areas of ECs exposed to d-flow (atheroprone) compared with areas exposed to l-flow (atheroresistant) (Figure 7C and Supplemental Figure 8). Similarly, we detected markedly higher levels of MAGI1 expression in d-flow areas than in l-flow areas of *Ldlr*<sup>-/-</sup> mice fed a high-fat diet (HFD). However, we found no statistically significant differences in the level of MAGI1 expression in d-flow areas between NC-fed WT and HFD-fed *Ldlr*<sup>-/-</sup> mice (Figure 7D). Furthermore, we examined MAGI1-S741 phosphorylation in NC-fed WT mice and found considerably greater MAGI1-S741 phosphorylation in d-flow areas compared with l-flow areas (Figure 7, E and F). In addition, this phosphorylated form of MAGI1 was predominantly localized in the nucleus (Figure 7F). These data support our in vitro findings of d-flow directing MAGI1 to the nucleus and the crucial role of MAGI1 S741 phosphorylation in atherosclerotic plaque formation.

Because the genome-wide association study described previously suggested a possible correlation between the MAGI1 locus and the severity of chronic inflammatory diseases, we measured the level of MAGI1 expression in human inflamed colonic tissue samples (Supplemental Table 2) by performing triple staining with anti-MAGI1 (red), anti-CD31 (green), and DAPI (blue). As shown in Figure 7, G and H, and Supplemental Figure 9, we observed substantially higher levels of MAGI1 expression at the luminal surface of human colonic epithelial samples obtained from Crohn disease (CD) and ulcerative colitis (UC) patients than in samples obtained from normal controls. Interestingly, nondividing differentiated cells are located at the luminal surface of the human colonic epithelium (32–34).

Next, we evaluated the colocalization of CD31 and MAGI1 signals in ECs by calculating the Pearson correlation coefficient at the sites of vessels in 6, 17, and 9 samples of colons obtained from non-IBD controls and CD and UC patients, respectively. We found markedly greater colocalization of MAGI1 with CD31 in CD samples (Pearson correlation coefficient,  $0.4989 \pm 0.0468$ , mean  $\pm$  SEM) than in normal samples ( $0.1675 \pm 0.06776$ , mean  $\pm$  SEM). Of note, we did not detect a significant increase in MAGI1 and CD31 colocalization in UC samples (Figure 7, G and I). This may be due to fewer samples with intact vessel formation than in the CD group. These data suggest that endothelial MAGI1 expression contributes to the process of CD progression. Furthermore, we examined the role of MAGI1 in Thb-induced NF- $\kappa$ B activation in human colonic epithelial cells and found that depletion of MAGI1 inhibited Thb-induced NF- $\kappa$ B activation (Figure 1F). Taken together, these data suggest a crucial role for MAGI1 in regulating inflamma-

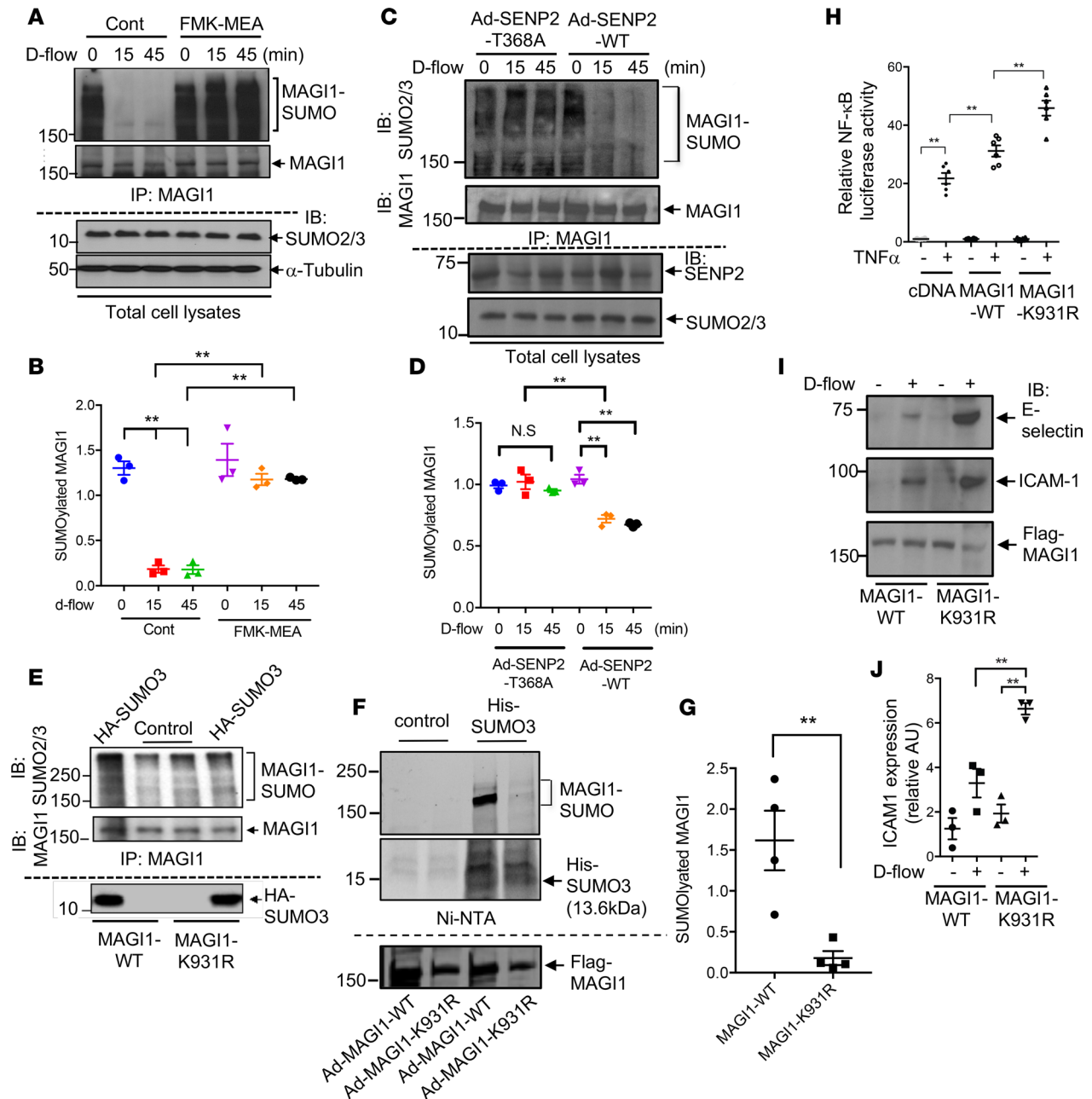


**Figure 5. MAG1 deSUMOylation associated with EC activation.** (A and B) HUVECs treated with FMK-MEA (10  $\mu$ M, 30 minutes) were exposed to d-flow, and the level of SUMOylated MAG1 was determined (first row above the dotted line). The membrane was then immunoblotted with an anti-MAG1 antibody (A, Sigma, rabbit polyclonal antibody [M5691], and B, Santa Cruz, mouse monoclonal antibody [SC-100326]) (second row above the dotted line), indicating pull-down of equal amounts of MAG1. The levels of SUMO2/3 and tubulin expression in cell lysates are shown in the rows below the dotted line. SUMOylated MAG1 levels were quantified by densitometry of immunoblots from 3 independent experiments and are plotted (B) ( $n = 3$ ). Data represent mean  $\pm$  SEM.  $**P < 0.01$ . Cont, control. (C) HUVECs transduced with Ad-SEN2-WT or -T368A were exposed to d-flow, and the level of SUMOylated MAG1, MAG1, SENP2, and SUMO2/3 expression was determined as in A. (D) Levels of SUMOylated MAG1 were quantified by densitometry of immunoblots from 3 independent experiments and are plotted (D) ( $n = 3$ ). Data represent mean  $\pm$  SEM.  $**P < 0.01$ . (E) The levels of SUMOylated MAG1, MAG1, and hemagglutinin-tagged (HA-tagged) SUMO3 expression in ECs coexpressing HA-tagged pcDNA-SUMO3 and pCMV-Flag-MAG1-WT or -K931R determined as in A. (F and G) HUVECs were transduced with Ad-Flag-MAG1 WT or Ad-Flag-MAG1 K931R mutant with His-tagged SUMO3 or a control vector. His-tagged SUMO3 was pulled down by Dynabeads and immunoblotted with anti-Flag (MAG1) and anti-His (SUMO3). (G) Quantification of pulled down SUMOylated MAG1 expression relative to that of Flag-MAG1 ( $n = 3$ ). Data represent mean  $\pm$  SEM.  $**P < 0.01$ . (H) ECs expressing pCMV-Flag-MAG1-WT or -K931R or a control vector were subjected to an NF- $\kappa$ B activity assay with TNF- $\alpha$  treatment (10 ng/ml, 24 h). The relative NF- $\kappa$ B luciferase activity was measured and presented as the mean  $\pm$  SEM ( $n = 6$ ).  $**P < 0.01$ . (I) Bovine aortic ECs expressing pCMV-Flag-tagged MAG1-WT or -K931R were exposed to d-flow for 12 hours, and the levels of E selectin, ICAM-1, and MAG1 expression were determined. (J) The intensity of ICAM-1 expression relative to that of tubulin expression was quantified. Data represent mean  $\pm$  SEM ( $n = 3$ ).  $**P < 0.01$ ;  $***P < 0.001$ . Statistical differences between 2 independent groups (G) were assessed using the Student's  $t$  test (2-tailed) and 1-way ANOVA followed by Bonferroni's post hoc testing for multiple groups (B, D, H, and J).

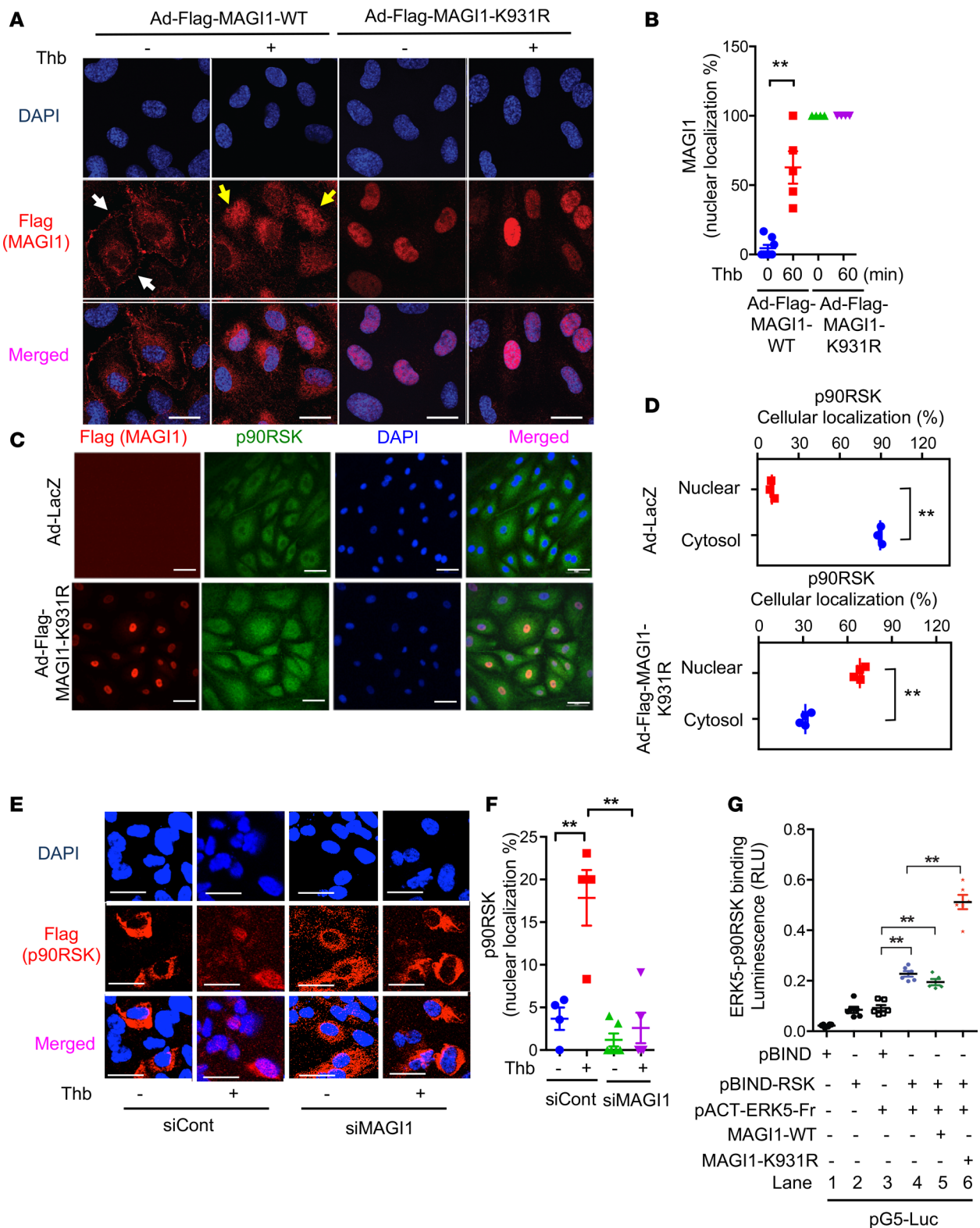


**Figure 6. MAGI1-K931 deSUMOylation induces nuclear translocation of MAGI1 and p90RSK.** (A) HUVECs transduced with Ad-Flag-MAGI1-WT or -K931R were treated with Thb (1 h) and then immunostained with an anti-Flag antibody (red). The cells were counterstained with DAPI to identify nuclei. Treatment with 10 U/ml Thb caused nuclear MAGI1 translocation (Ad-Flag-MAGI1-WT images). MAGI1-K931R was localized exclusively in the nucleus even in the absence of inflammatory stimulation (Ad-Flag-MAGI1-K931R images). MAGI1 was localized at the cell membrane (white arrows) under unstimulated conditions and in the nucleus (yellow arrows) after Thb treatment. (B) Quantification of the percentage of nuclear MAGI1 localization, as described in Methods. Data represent mean  $\pm$  SEM ( $n = 5-9$ ).  $**P < 0.01$ . (C) HUVECs transduced with Ad-Flag-MAGI1-K931R or Ad-LacZ were coimmunostained with an anti-Flag antibody (red) and anti-p90RSK antibody (green). p90RSK staining was cytoplasmic in cells transduced with Ad-LacZ but nuclear in cells transduced with Ad-Flag-MAGI1-K931R. (D) Quantification of the percentage of cellular p90RSK localization, as

described in Methods. Data represent mean  $\pm$  SEM ( $n = 3$ ).  $^{**}P < 0.01$ . Scale bars: 20  $\mu\text{m}$ . (**E** and **F**) HUVECs treated with MAGI1 or control siRNA were transduced with Ad-Flag p90RSK and stimulated with Thb (1 h). Thb induced nuclear p90RSK localization, as indicated by immunostaining of cells with an anti-Flag antibody; p90RSK nuclear translocation was inhibited by MAGI1 siRNA (siMAGI1). (**F**) Quantification of the percentage of nuclear p90RSK localization, as described in Methods. Data represent mean  $\pm$  SEM ( $n = 3$ ).  $^{**}P < 0.01$ . Adenoviral transduction: MOI, 20. siCont, control siRNA. (**G**) Results of a CheckMate Mammalian Two-Hybrid assay showing increased p90RSK-ERK5 binding in HUVECs expressing the MAGI1-K931R mutant. p90RSK-ERK5 binding was detected when p90RSK and the ERK5 fragment (amino acid 571–807 fragment) (17) were coexpressed (lanes 4 and 5), and the binding was enhanced by MAGI1-K931R overexpression (lane 6). Data represent mean  $\pm$  SEM ( $n = 5$ –6). RLU, relative light units.  $^{**}P < 0.01$ . Statistical differences between 2 independent groups (**D**) were assessed using the Student's *t* test (2-tailed) and 1-way ANOVA followed by Bonferroni's post hoc testing for multiple groups (**B**, **F**, and **G**).

tion in both ECs and colonic epithelial cells and supports a possible role for MAGI1 in IBD progression.

*MAGI1 regulates ER stress signaling and apoptosis via formation of a complex with ATF6.* To further understand the biological implications of MAGI1 expression in ECs, we transfected HUVECs with control or *Magi1* siRNA, exposed them to d-flow, and isolated and transcriptionally profiled their total RNA (Supplemental Figure 10A). We submitted a set of genes with significantly different expression levels in ECs (absolute fold change  $> 2$ ;  $P < 0.05$ ) to Ingenuity Pathway Analysis (IPA; QIAGEN). Using Fisher's exact test enrichment analysis for curated gene sets categorized according to biological function and disease, we found that gene sets in the Immunological Disease, Antimicrobial Response, Inflammatory Response, and Infectious Disease categories were among the 5 most significantly different in gene expression set categories ( $-\log[P] > 20$ ) (Supplemental Figure 10B). Based on the directional gene expression changes and literature-substantiated causal relationships among each molecule, the gene enrichment calculations and predicted biological gene effects demonstrated that gene expression predicted reduced granulocyte activation in *Magi1* siRNA-transfected ECs under d-flow conditions but not in control ECs (*Z*-score,  $-2.969$ ;  $P = 9.96 \times 10^{-5}$ ) (Supplemental Figure 10C).

Following IPA network generation, which is optimized for interconnectivity of differentially expressed genes under the constraint of a maximal network size, we carried out Fisher's exact test and Gene Set Enrichment Analysis (GSEA) to identify the biological functions expected to be affected by a given interaction network. Gene set function and disease enrichment of the top-ranked interaction networks based on the number of interconnected differentially expressed genes identified the gene set categories with the lowest *P* values as Cardiovascular Disease, Organism Injury and Abnormalities, and Reproductive System Disease (25 differentially expressed genes) (Figure 8A and Supplemental Table 3). Our analysis of the Cardiovascular Disease network using IPA demonstrated that ER stress-related X-box binding protein 1 (XBP-1) is a hub molecule in this network and that MAGI1 depletion downregulates d-flow-induced expression of ER stress-related genes, including *XBPI* and eukaryotic translation initiation factor 2  $\alpha$  kinase 3 (also known as pancreatic EIF2- $\alpha$  kinase), in ECs (Figure 8A and Supplemental Table 3). We verified reduced expression of certain molecules shown in Figure 8A, such as XBP-1, spliced XBP-1 (Figure 8B), and TNFSF15 (Figure 8C), using quantitative reverse transcription-PCR (qRT-PCR). Because d-flow increases EC apoptosis by upregulating spliced XBP-1 expression and enhances atherosclerotic plaque formation (35), we examined EC apoptosis and found that d-flow-induced apoptosis was inhibited in *Magi1* siRNA-treated ECs compared with that in control siRNA-treated ECs (Figure 8D).

To define how MAGI1 can regulate ER stress signaling, we sought to determine whether MAGI1 can associate with activating transcription factor 6 (ATF6), an upstream transcription factor for XBP-1. We found that both murine and human MAGI1 can associate with ATF6 using a mammalian 2-hybrid assay (Figure 8E and Supplemental Figure 11A). We also found that treatment with Thb increased the association of MAGI1 with ATF6 (especially the cleaved form of ATF6) using co-IP with an anti-Flag antibody (MAGI1) and IB with an anti-ATF6 antibody (Figure 8, F and G). ATF6 cleaved by site 1 and 2 proteases is well known to be able to translocate from the ER and Golgi apparatus to the nucleus, bind to ER stress response elements, and upregulate XBP-1 expression (36). Bands of ATF6 in HUVECs on Western blots were confirmed by depleting ATF6 expression with siRNA (full length, 75 kDa and 90 kDa, and cleaved form, 47 kDa) (Supplemental Figure 11B). Because depletion of MAGI1 inhibited d-flow-induced XBP-1 expression and d-flow- and Thb-induced MAGI1 and ATF6 interaction, we examined whether MAGI1 plays a crucial role in nuclear ATF6 translocation after Thb stimulation. As shown in Figure 9, A and B, nuclear ATF6 translocation induced by Thb was significantly inhibited by MAGI1 siRNA. In addition, overexpressed MAGI1-K931R increased shuttling of ATF6 to the nucleus (Supplemental Figure 11C). Of note, the anti-ATF6 antibody used in these experiments can recognize full-length and cleaved forms of ATF6. We observed nuclear ATF6 translocation within 1 hour after Thb stimulation without increased cleaved ATF6 expression, suggesting a crucial

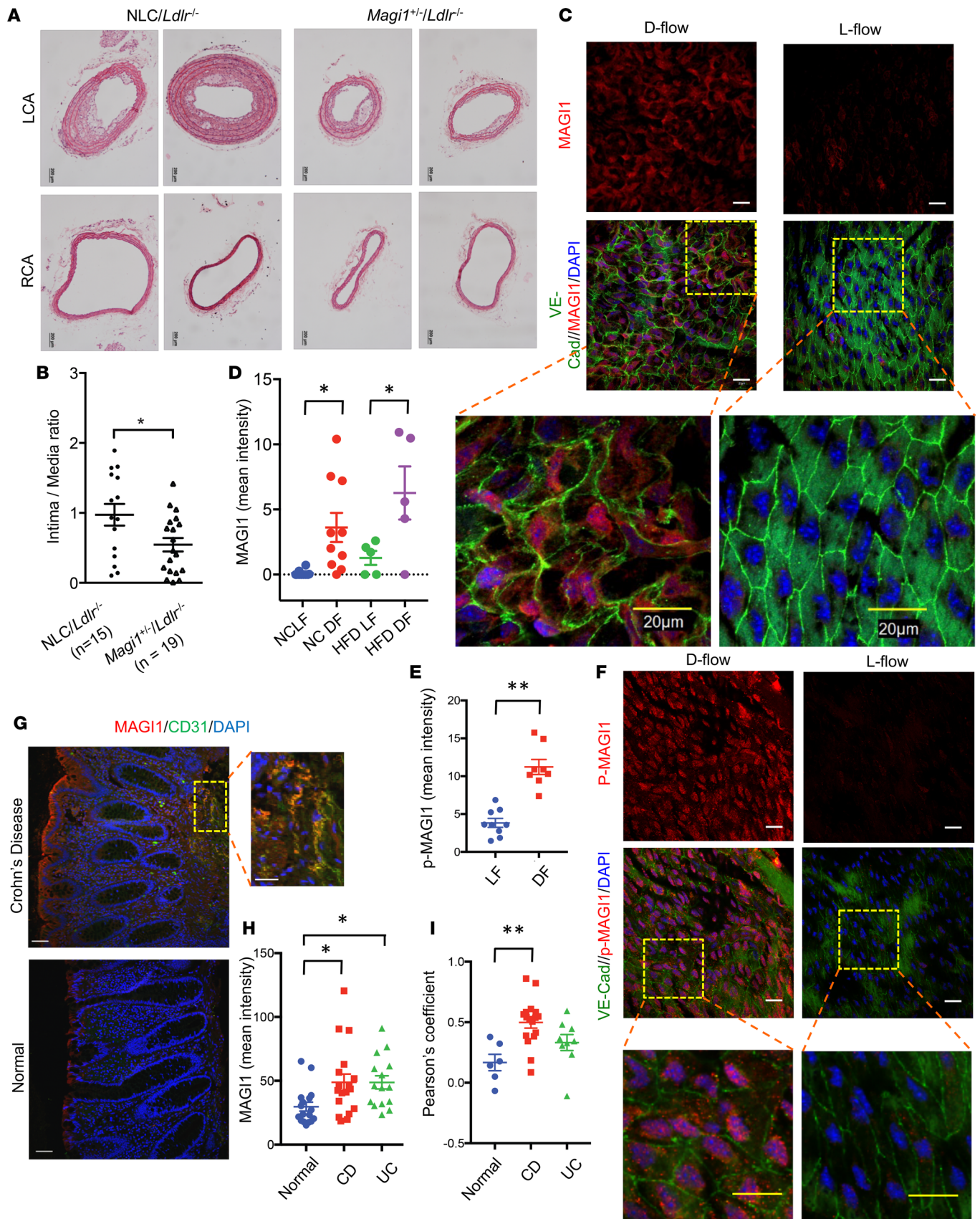


**Figure 7. MAGI1 expression in d-flow–induced atherosclerosis and in colonic tissues of IBD patients.** (A) Representative images of H&E-stained sections of LCA and RCA samples obtained from *NLC/Ldlr<sup>-/-</sup>* and *Magi1<sup>-/-</sup>/Ldlr<sup>-/-</sup>* mice after 4 weeks of partial LCA ligation. Scale bars: 200  $\mu$ m. (B) The intima/media ratios in H&E-stained LCA sections (18). Data represent mean  $\pm$  SEM for *NLC/Ldlr<sup>-/-</sup>* ( $n = 15$ ) and *Magi1<sup>-/-</sup>/Ldlr<sup>-/-</sup>* ( $n = 19$ ) mice. \* $P < 0.05$ . (C and D) Aortas were harvested from *Magi1<sup>-/-</sup>/Ldlr<sup>-/-</sup>* HFD-fed mice. En face preparations of aortas were coimmunostained with anti-VE-cadherin (green) and -MAGI1 (red) antibodies. (C) Aorta areas exposed to l-flow or d-flow. The boxed areas are magnified below. Scale bars: 20  $\mu$ m. (D) Histogram of MAGI1 staining in d-flow (DF) and l-flow (LF) regions in NC-fed WT mice and HFD-fed *Ldlr<sup>-/-</sup>* mice. Data represent mean  $\pm$  SEM ( $n = 5$ –10/group). \* $P < 0.05$ . (E and F) Aortas were harvested from NC-fed WT C57BL/6 mice. (F) En face preparations of aortas were coimmunostained with anti-VE-cadherin (green) and anti-phospho-specific MAGI1-S741 (red) antibodies. (E) Histogram of phospho-specific MAGI1-S741 staining. Data represent mean  $\pm$  SEM ( $n = 8$ –10/group). \*\* $P < 0.01$ . (G–I) Paraffin-embedded sections of colonic tissue samples obtained from patients with UC or CD and control patients without IBD were immunostained with anti-MAGI1 (red), anti-CD31 (green), and DAPI (blue). (G) More intense MAGI1 staining at the luminal surface in colonic epithelium samples obtained from CD and UC patients compared with those obtained from normal controls. The boxed area is magnified at right and shows colocalization of CD31 and MAGI1. Scale bars: 50  $\mu$ m; 20  $\mu$ m (zoom inset). (H) The intensity of the MAGI1 staining at the luminal surface in each sample was determined using ImageJ. Data represent mean  $\pm$  SEM ( $n = 15$ –18/group). \* $P < 0.05$ . (I) Colocalization of CD31 and MAGI1 at the vessels in the samples was assessed using Pearson's correlation coefficient. CD31 staining structures were excluded when we could not clearly identify them as vessels. Data represent mean  $\pm$  SEM ( $n = 6$ –17/group). \*\* $P < 0.01$ . Statistical differences between 2 independent groups (B and E) were assessed using the 2-tailed Student's *t* test and 1-way ANOVA followed by Bonferroni's post hoc testing for multiple groups (D, H, and I).

role for MAGI1 SUMOylation in regulating nuclear ATF6 translocation via a cleaved ATF6-independent mechanism. Next, to determine the role of ATF6 in p90RSK-MAGI1–induced EC apoptosis, we depleted ATF6 from ECs with siRNA and transduced the cells with Ad-MAGI1-WT, Ad-MAGI1-K931R mutant, Ad-WT-p90RSK, or Ad-LacZ (control) as indicated (Figure 9, C and D). Co-overexpression of WT-p90RSK with MAGI1-K931R resulted in considerably higher apoptosis than co-overexpression with MAGI1-WT. This effect was significantly inhibited by ATF6 knockdown, suggesting a crucial role for ATF6 in MAGI1 and MAGI1 SUMOylation-mediated apoptosis induced by p90RSK activation (Figure 9, C and D). Taken together, these data propose a critical role for MAGI1 in nuclear ATF6 translocation via formation of a MAGI1-ATF6 complex that induces XBP-1 expression and apoptosis in ECs.

## Discussion

In the present study, we showed that MAGI1 is essential for the regulation of endothelial activation. We made several potentially new findings: (a) a role for MAGI1 as a piggyback carrier of p90RSK and ATF6 from the cytosol to the nucleus, (b) p90RSK-mediated MAGI1 phosphorylation and deSUMOylation as crucial events that lead to EC activation, and (c) the introduction of the possibly novel concept that MAGI1, together with p90RSK, regulates EC activation and apoptosis via cytosolic Rap1 activation and promotion of the nuclear translocation of p90RSK and ATF6 (Figure 9E). Of note, deletion of MAGI1 in MLECs, HUVECs, and human colonic epithelial cells abolished not only d-flow– but also TNF- $\alpha$ –induced NF- $\kappa$ B activation and VCAM-1 expression (Figure 1). These findings suggest that MAGI1 is a major but unexplored molecule that regulates EC activation. We believe that the concept of MAGI1 PTM-elicited EC activation is novel and highlights the importance of intracellular localization-dependent events coordinately regulated by inflammatory inputs, such as d-flow, that cause EC activation and ER stress–induced apoptosis. Furthermore, our study revealed that MAGI1 expression was increased in the colonic epithelium and endothelium of human IBD samples as well as in ECs at d-flow areas of the aortic arch. Moreover, depletion of MAGI1 significantly inhibited d-flow–induced atherosclerotic plaque formation. Based on these findings, we propose that MAGI1 is an attractive drug target, especially by modifying MAGI1 PTM, for parallel control of EC activation and ER stress–induced apoptosis.

The association of EC activation with cardiovascular diseases is well established. At the basic science level, an understanding of the specific signaling events involved in the mechanism of EC activation is key to the development of therapeutic strategies against vascular disease. A recent study by our group demonstrated that p90RSK is activated by d-flow but not by l-flow (18). This suggests that upon activation, p90RSK induces MAGI1-S741 phosphorylation in areas of d-flow, which in turn increases the severity of inflammatory responses to ECs located in those areas. Our data on the inhibition of d-flow–induced MAGI1 deSUMOylation by the SENP2-T368A mutant (Figure 5, C and D) also indicate possible involvement of p90RSK-mediated nuclear SENP2 export in cytoplasmic MAGI1 deSUMOylation, causing translocation of the p90RSK-MAGI1 complex to the nucleus. We found that overexpression of a p90RSK-MAGI1-binding inhibitory fragment abolished Thb-induced adhesion molecule expression (Figure 2G), suggesting an essential role for p90RSK-MAGI1 complex formation in regulation of d-flow–induced EC activation. Although the functional role of p90RSK in the nucleus is established, the exact mechanism of nuclear

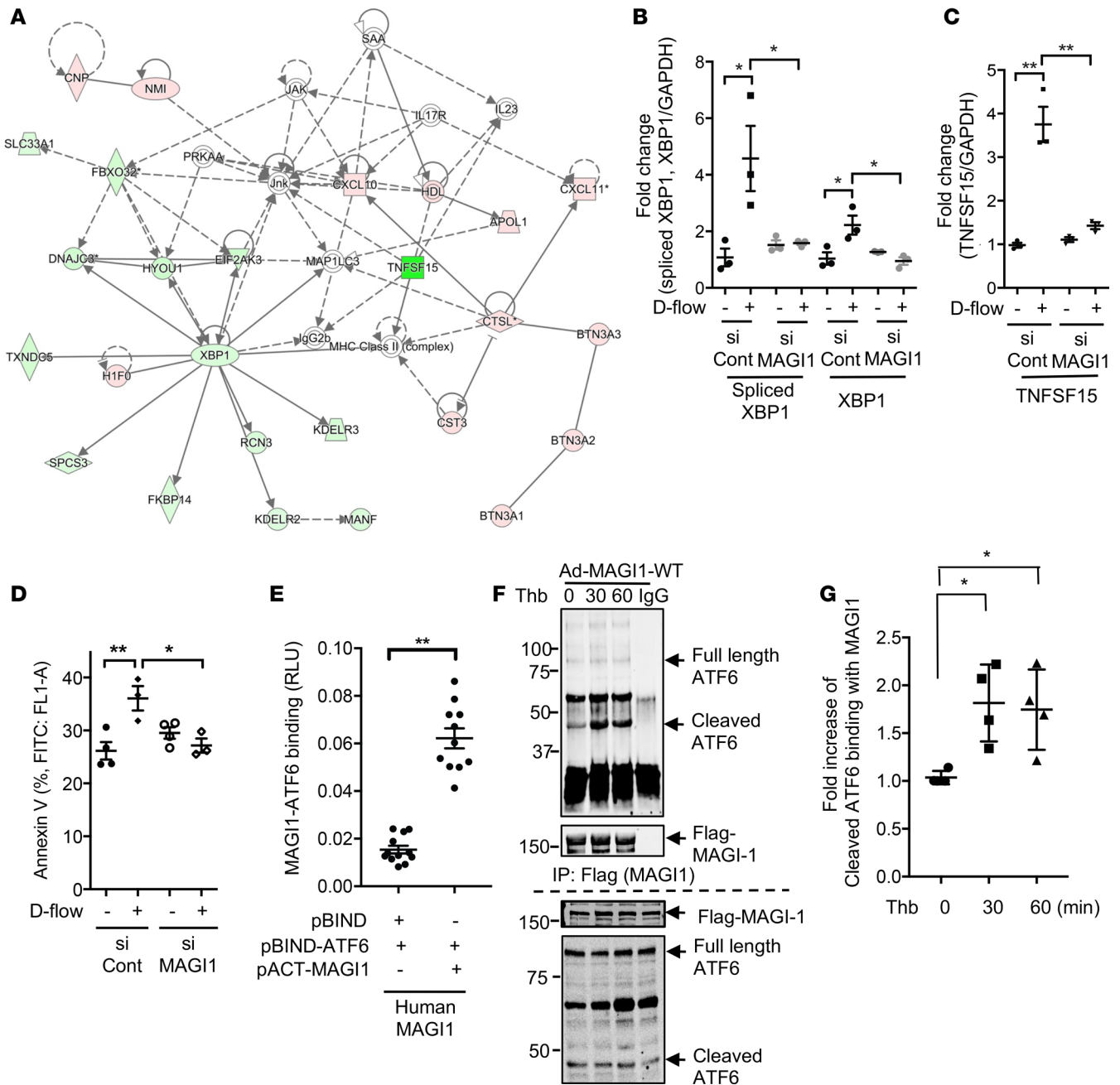


**Figure 8. MAGI1 regulates d-flow-induced XBP-1 expression.** (A) Gene enrichment analyses (right-tailed Fisher's exact test) were performed according to IPA downstream effect analysis, and we identified Cardiovascular Disease, Organism Injury and Abnormalities, and Reproductive System Disease as the highest scoring IPA interaction networks in our microarray data set. Green and red symbols denote genes with lower and higher expression, respectively, in MAGI1 siRNA-treated ECs compared with that in control siRNA-treated cells. The arrows with solid lines indicate direct (usually physical) interactions between two molecules in the direction of the arrows, whereas arrows with dashed lines denote indirect interactions (e.g., molecule/gene A affects molecule/gene B). The abbreviations are defined in Supplemental Table 3. (B and C) Levels of spliced and total *Xbp1* (B) and *Tnfsf15* (C) mRNA expression were reduced in MAGI1 siRNA-treated (siMAGI1-treated) ECs under d-flow stimulation. Data represent mean  $\pm$  SEM ( $n = 3$ ). \* $P < 0.05$ ; \*\* $P < 0.01$ . siCont, control siRNA. (D) d-flow-mediated EC apoptosis was inhibited by treatment with MAGI1 siRNA. Data represent mean  $\pm$  SEM ( $n = 3-4$ ). \* $P < 0.05$ ; \*\* $P < 0.01$ . (E) MAGI1-ATF6 binding was assessed using a CheckMate Mammalian Two-Hybrid Assay. Human aortic endothelial cells (HAECS) were transfected with human pACT-MAGI1, pBIND-ATF6, and a luciferase reporter vector (PG5-Luc), and their luciferase activity was measured. Relative MAGI1-ATF6 binding data are presented as firefly/Renilla luciferase activity ratios. Data represent mean  $\pm$  SEM ( $n = 12$ ). RLU, relative light units. \*\* $P < 0.01$ . (F and G) HAECS transduced with Ad-Flag-MAGI1-WT were treated with Thb (10 U/ml) for 16 hours. MAGI1-ATF6 binding was measured via co-IP with anti-Flag followed by IB with anti-ATF6 and then anti-Flag to confirm that equal amounts of protein were pulled down. The rows below the dotted line in F show Flag-MAGI1 and ATF6 levels in the total cell lysates. These are representative figures from 6 different experiments. Quantification data are shown in G. \* $P < 0.05$  (G). Data represent mean  $\pm$  SEM ( $n = 6$ ). Statistical differences between 2 independent groups (E) were assessed using the Student's *t* test (2-tailed) and 1-way ANOVA followed by Bonferroni's post hoc testing for multiple groups (B, C, D, and G).

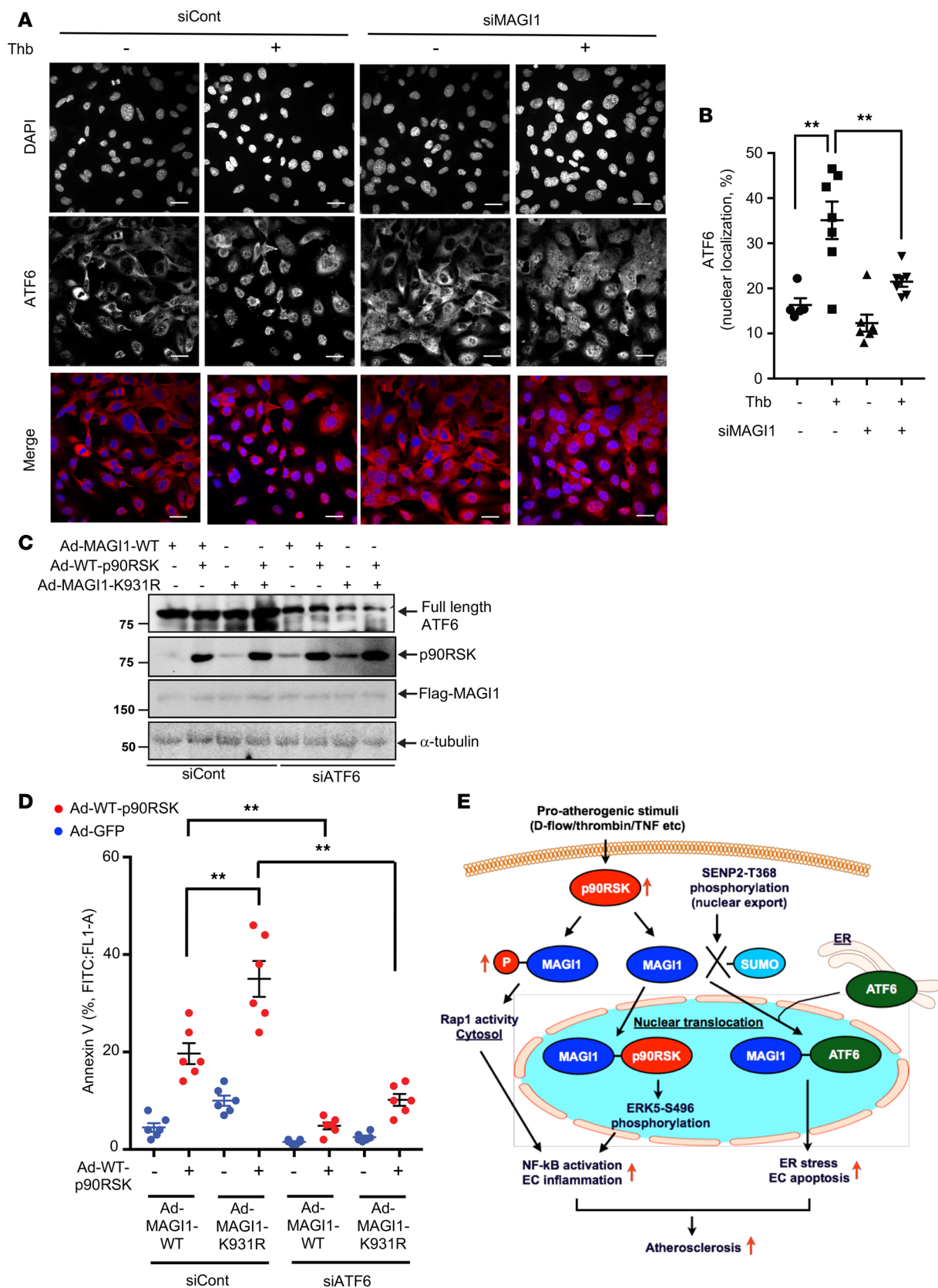


**Figure 9. MAG1 regulates nuclear ATF6 translocation induced by treatment with Thb.** (A and B) HUVECs treated with siRNA were stimulated with Thb (1 h). Thb induced nuclear ATF6 localization, as indicated by immunostaining of cells with anti-ATF6. ATF6 nuclear translocation was inhibited by treatment with MAG1 siRNA (siMAG1). Scale bars: 20  $\mu$ m. (B) Quantification of the percentage of cells with nuclear ATF6 localization. Data represent mean  $\pm$  SEM.  $^{***}P < 0.01$ . siCont, control siRNA. (C and D) HUVECs were treated with ATF6 or control siRNA for 48 hours and transduced with an adenovirus containing WT p90RSK (Ad-WT-p90RSK), MAG1-WT (Ad-WT-MAG1), the MAG1-K931R mutant (Ad-MAG1-K931R), or LacZ as a control. p90RSK, MAG1, and ATF6

expression were detected using Western blotting, as indicated in **C**. Sixteen hours later, EC apoptosis was evaluated according to annexin V expression, as described in Methods. Data represent mean  $\pm$  SEM ( $n = 6$ )  $**P < 0.01$ . **(E)** Schematic of the role of MAGI1 PTMs in regulation of EC activation. Proatherogenic stimuli activate p90RSK, independently increasing MAGI1-S741 phosphorylation and MAGI1-K931 deSUMOylation. MAGI1-S741 phosphorylation increases Rap1 activation in the cytosol, whereas MAGI1-K931 deSUMOylation induces nuclear cotranslocation of the p90RSK- or ATF6-MAGI1 complex and instigates nuclear events such as increased binding of nuclear p90RSK to ERK5, which inhibits the atheroprotective function of ERK5, and XBP-1 expression induced by nuclear ATF6 translocation. These events lead to EC activation and apoptosis and subsequent atherosclerotic plaque formation. X, disruption of MAGI1 SUMOylation. Statistical differences were assessed using 1-way ANOVA followed by Bonferroni's post hoc testing for multiple groups.

p90RSK translocation remains unclear. Our study proposes a possibly novel process in which p90RSK piggybacks with de-SUMOylated MAGI1 into the nucleus, eliciting inflammatory responses in ECs via SENP2-T368 phosphorylation and nuclear p90RSK-ERK5 association. Furthermore, we found that MAGI1-S741A inhibited d-flow-induced Rap1 and subsequent NF- $\kappa$ B activation in ECs. To the best of our knowledge, no other studies have focused on p90RSK-regulated PTMs of MAGI1 as unique proinflammatory events in ECs that lead to atherosclerotic plaque formation.

PTMs are dynamic processes that, among other roles, are involved in regulating substrate intracellular localization. Specifically, PTMs can promote rapid shuttling of substrates across the nuclear membrane. We, and others, reported on the crucial role of p53 SUMOylation in regulating the nuclear export of p53 by SENP2 (37, 43, 44). Being a dynamic process, SUMOylation substrates exist in a cycle of SUMOylation and deSUMOylation, and, under certain conditions, one state may become favored over the other. For example, under d-flow stimulation, MAGI1 deSUMOylation is favored, which results in nuclear translocation of MAGI1. It is noteworthy that, although the modified amount of a specific substrate is low in stoichiometry, the biological consequence can be considerable. For example, phosphorylation of ERK1/2 causes it to translocate into the nucleus, resulting in cellular proliferation; however, the stoichiometry between phosphorylated and unphosphorylated ERK1/2 is low to moderate (37, 38). Similarly, deSUMOylation-mediated MAGI1 nuclear translocation may exert a significant biochemical effect on the nucleus, even when the SUMOylated form of MAGI1 is predominant in the cell.

The crucial role of ER stress in d-flow-induced atherogenesis has been reported. For example, Civelek et al. (39) reported upregulation of expression of the ER stress-related signaling molecules, such as inositol-requiring transmembrane kinase/endonuclease 1, ATF6, and XBP-1, at d-flow areas of the swine aortic arch. In addition, Zeng et al. (35) reported that d-flow increased both full-length and spliced XBP-1 expression, leading to EC apoptosis by inhibiting VE-cadherin expression. In addition, overexpression of XBP-1 accelerated atherosclerotic plaque formation. In the present study, using microarray screening, we found that ER stress-related signaling can be a downstream target of MAGI1. Both full-length and spliced XBP-1 expression were increased by d-flow as reported previously (35), and depletion of MAGI1 completely inhibited d-flow-induced XBP-1 and spliced XBP-1 expression and subsequent EC apoptosis. Of note, we found that MAGI1 can directly associate with ATF6, which is one of the ER-proximal unfolded-protein response transmembrane proteins, and regulates the nuclear translocation of ATF6. Overexpression of the MAGI1-K931R mutant increased nuclear ATF6 translocation (Supplemental Figure 11C) and WT-p90RSK-mediated apoptosis, which was significantly inhibited by ATF6 siRNA transfection (Figure 9D). These data suggest a crucial and possibly unique role for MAGI1 in nuclear translocation of both p90RSK and ATF6 via a piggyback system and that nuclear p90RSK and ATF6 regulate EC activation and apoptosis, respectively.

In the present study, we found that MAGI1 is essential for NF- $\kappa$ B activation in ECs induced by various proinflammatory stimuli. While it remains unclear whether a single-nucleotide polymorphism or deletion close to the MAGI1 gene as previously reported (4, 5) can increase MAGI1 expression in humans, our study demonstrates that both PTMs and expression of MAGI1 have a significant effect on EC activation as well as atherosclerotic plaque formation. Further studies are necessary to determine whether the single-nucleotide polymorphism in the first intron of *Magi1* or the intergenic deletion between the *Adams9* and *Magi1* genes at the chromosome 3p14.1 locus can change MAGI1 expression or PTMs in ECs and/or epithelial cells.

There are several limitations of this study. Although we found increased MAGI1 expression in IBD histological samples and d-flow area, the molecular mechanisms for this remain unclear. In particular, it is intriguing that HFD did not increase MAGI1 expression compared with NC diet (Figure 7D), suggesting that d-flow may elicit some unique signaling beside the inflammatory responses and increase MAGI1 expression, but further investigation is necessary. Furthermore, the potential role of MAGI1 in regulating permeability

together with junctional adhesion molecule 4 (JAM4) has been suggested (40), but how MAGI1 PTMs affect EC permeability is yet to be determined. Our current study showed the crucial role of MAGI1 PTMs in simultaneously regulating EC activation and ER stress-mediated apoptosis and poses MAGI1 as an attractive therapeutic target to inhibit atherosclerosis and subsequent adverse cardiovascular events. There were no additive effects of complete depletion (homozygous) or partial inhibition (heterozygous) of MAGI1 on d-flow-induced atherosclerotic plaque formation, probably due to increased EC permeability owed to complete MAGI1 deletion, because the increase of EC permeability may enhance the atherosclerosis formation (41). We plan to investigate the role of MAGI1 and its PTMs in regulating EC permeability in future studies.

## Methods

Additional details concerning the experimental procedures are included in the Supplemental Methods.

**Mice.** Mice were housed in a pathogen-free environment at the Texas A&M Institute of Biosciences and Technology. *Magi1*<sup>-/-</sup> mice were generated by Lexicon Pharmaceuticals using gene-trap insertion (*Magi1*<sup>Gt(OST33326)Lex</sup>) in a C57BL/6 background. To generate an atherosclerosis model, male *Magi1*<sup>-/-</sup> mice were crossed with *Ldlr*<sup>-/-</sup> mice (The Jackson Laboratory) to obtain *Magi1*<sup>+/-</sup>/*Ldlr*<sup>-/-</sup> and NLC/*Ldlr*<sup>-/-</sup> (*Magi1*<sup>+/-</sup>/*Ldlr*<sup>-/-</sup>) mice. Eight- to twelve-week-old mice were fed an adjusted-calorie HFD consisting of 21% crude fat, 0.15% cholesterol, and 19.5% casein (Envigo, TD.88137) (17). To determine the functional role of MAGI1 in ECs, both *Magi1*<sup>-/-</sup> and *Magi1*<sup>+/-</sup> mice were used in in vitro studies (VCAM-1 expression), and similar tendencies of antiinflammatory effects were observed for the 2 genotypes.

**Partial LCA ligation.** In vivo studies of d-flow-induced atherosclerosis were performed using a partial LCA ligation mouse model in which the left internal and external carotid arteries were ligated using a 6-0 silk suture but the occipital artery was left intact. Four weeks after ligation, the LCA and RCA were harvested, fixed, embedded in paraffin, serially sectioned (5 μm), and stained with H&E, and the intima/media ratio in LCA was determined using ImageJ (NIH). The intimal area was calculated by subtracting the luminal area from the area circumscribed by the internal elastic lamina, whereas the medial area was the area between the internal and external elastic laminae (18). Based on previous reports (42), a series of 10 cross sections (5 μm) every 200 μm over a 3.5-mm length of carotid artery beginning at the origin defined according to bifurcation morphology was analyzed (total 14 divisions from 1 carotid; total number of cross sections from 1 carotid was 140 cross sections). Two or three sections from one division were analyzed, and the mean area of intima and media for each of 14 divisions of LCA and RCA was calculated in every animal (43).

**Human colonic tissue samples and staining.** Samples of human colons were retrospectively obtained from the Mayo Clinic. Specifically, biopsy samples were collected during routine endoscopy, and surgically resected samples were obtained from IBD and non-IBD patients. Control non-IBD samples were obtained from normal regions of bowel adjacent to resected colorectal tumors. Samples were fixed in buffered formalin, embedded in paraffin, and sectioned. Paraffin slides were baked for approximately 1 hour at 60°C, and then deparaffinized and rehydrated. Antigenicity was retrieved via HIER with 10 mM sodium citrate buffer, pH 6. Sections were then blocked overnight in 10% normal goat serum. Primary antibodies, MAGI1 at 1:100 (Abcam, ab37543) and CD31 (JC/70A) at 1:100 (Invitrogen, MA5-13188), or IgG control were applied and incubated overnight at 4°C. The following day secondary antibodies, AF546 goat-anti rabbit IgG (Invitrogen, A11029) at 1:1000, AF488 goat anti-mouse (Invitrogen, A11035) at 1:1000, and DAPI (Invitrogen, D1306) at 1:2000, were applied for 1 hour, and the sections then mounted with ProLong Gold (Invitrogen, P36934) prior to imaging. For each subject, 3 sections were stained, and the mean intensity of each staining was calculated. To compare MAGI1 expression levels in the samples, the area occupied by colonic crypts and stroma was identified based on DAPI staining and the faint autofluorescence of the tissue, and the average anti-MAGI1 staining intensity per unit area for each slide was measured using ImageJ (NIH) (44). See Supplemental Table 5 for all antibodies used in this study.

**qRT-PCR.** Total RNA was obtained from ECs using RNeasy columns with DNA digestion (QIAGEN, 74136) according to the manufacturer's instructions and reverse-transcribed first-strand cDNA by incubating in a 50-μl reaction mixture containing 1 μg purified RNA, 5 μl 10× buffer, 11 μl MgCl<sub>2</sub>, 10 μl dNTPs, 2.5 μl of a random hexamer, 1.25 μl oligo-dT, 1 μl of an RNase inhibitor, and 0.75 μl of a reverse transcriptase enzyme (TaqMan Reverse Transcription Reagents; made for Applied Biosystems by Roche Molecular Diagnostics, N808-0234) at 25°C for 10 minutes followed by 37°C for 60 minutes, 42°C for 60 minutes, and 95°C for 5 minutes before soaking at 4°C in a PCR cyclor. In some cases, an iScript cDNA synthesis Kit (Bio-Rad) was used instead of TaqMan Reverse Transcription Reagents. Target

cDNA levels were quantified using a CFX Connect Real-Time PCR Detection System (Bio-Rad). All reaction mixtures (10  $\mu$ l each) contained cDNA synthesized from 20 ng total RNA, 5  $\mu$ l iQ SYBR Green Supermix (Bio-Rad, 1708882), and 0.5  $\mu$ mol/l each forward and reverse primers (Supplemental Table 4). RT-PCR was carried out initially at 95°C for 3 minutes, followed by 40 cycles of denaturation at 95°C for 10 seconds and annealing at 55°C for 30 seconds. RT-PCR analysis of total and spliced XBP-1 was performed initially at 95°C for 3 minutes, followed by 40 cycles of denaturation at 95°C for 10 seconds, annealing at 62°C for 15 seconds, and extension at 72°C for 30 seconds, as reported by van Schadewijk et al. (45) using primers designed to span the 26-bp intron removed by using inositol-requiring transmembrane kinase/endonuclease 1, as described by Hirota et al. (46) and van Schadewijk et al. (45).

Fold changes in RNA expression were calculated using the  $\Delta\Delta$ Ct method (47). The primer sequences are listed in Supplemental Table 4.

*D-flow studies.* D-flow studies were performed using a cone-and-plate apparatus as we described previously (20).

*Gene expression profiling.* Total RNA was obtained from ECs using RNeasy columns (QIAGEN) with DNA digestion according to the manufacturer's instructions and subsequently hybridized using a GeneChip Human Transcriptome Array 2.0 (Affymetrix). The array data were incorporated into the Transcriptome Analysis Console 3.0 (Affymetrix), and GeneChip data were normalized using Tukey's biweight average algorithm and represented as a biweight average on a  $\log_2$  scale. Significant differences between 2 groups were identified using unpaired ANOVA ( $P < 0.05$ ) with  $\log_2$ -transformed normalized intensities, and transcripts with greater than 2-fold differences in expression and  $P$  values of less than 0.05 were selected for each comparison analyzed. Data were analyzed using IPA (application build 377306M [2016-03-16] and content version 27216297 [2016-03-16]; QIAGEN). Fisher's exact test enrichment scoring and predicted activity states determined by using  $Z$ -score calculations based on correlated gene expression changes with literature-substantiated gene effects were used to identify statistically significant and activated states of canonical pathways, biological functions and disease, and predicted upstream transcriptional regulators ([http://pages.ingenuity.com/rs/ingenuity/images/0812%20downstream\\_effects\\_analysis\\_whitepaper.pdf](http://pages.ingenuity.com/rs/ingenuity/images/0812%20downstream_effects_analysis_whitepaper.pdf)). IPA interaction networks were based on gene or molecule connectivity with other genes and molecules in the analyzed data set (48). All molecular interactions and relationships of molecules with functions or diseases were based on curated findings in the literature stored in the Ingenuity Knowledge Base (QIAGEN).

*Data availability.* The microarray data and MAGI1 sequence were deposited in the NCBI's Gene Expression Omnibus database (accession GSE95066) and GenBank (accession KY651081), respectively. All other data supporting the findings of this study are available within the article or its supplemental materials.

*Statistics.* Statistical differences between 2 independent groups were assessed using the 2-tailed Student's  $t$  test and 1-way ANOVA followed by Bonferroni's post hoc testing for multiple group comparisons using Prism software (GraphPad Software). The differential expression in gene sets was assessed using right-tailed Fisher's exact test and Gene Set Enrichment Analysis (GSEA).  $P$  values less than 0.05 were considered statistically significant.

*Study approval.* All animal procedures were approved by the Institutional Care and Use Committees of the Texas A&M Institute of Biosciences and Technology (2014-0231, 2017-0154, Houston, Texas, USA) and The University of Texas MD Anderson Cancer Center (00001652, 00001109). Approval of human colonic tissue sample collection for experiments was obtained from the Mayo Clinic Institutional Review Board. All participants signed an IRB-approved informed consent form for IBD Biobank 13-000712.

## Author contributions

JA, KAK, JPM, YW, IJS, SK, MI, HTV, YT, MMLJ, TNT, JLM, JHW, YF, CJG, EM, JHS, LG, RJA, KF, and NTL generated animals, performed experiments, and analyzed data. WF provided IBD samples and made suggestions for the IBD study. JA, JT, KF, SEE, and NTL conceived and designed the experiments. JPC made suggestions for the study design and experiments. CJG and NM generated MAGI1 constructs. KAK, IJS, and TNT performed the animal experiments. JA, KF, and NTL wrote the manuscript. JT provided FMK-MEA and commented on the study design. All authors commented on the manuscript.

## Acknowledgments

We thank Darryl Gietzen and Alan Silverman for assistance with microarray data analysis; Ghiara Lugo Diaz, Mariana Roman, and Raymundo A. Quintana Quezada for assistance with microarray data validation; and Jessica J. Fritton for obtaining IBD samples. This work was supported in part by funding from the NIH to JA (HL-130193 and HL-134740), JPC (HL133254), and NTL (HL-134740) and the American Heart Association to NTL (AHA 13SDG14500033).

Address correspondence to: Jun-ichi Abe, Keigi Fujiwara, or Scott E. Evans, University of Texas MD Anderson Cancer Center, 2121 West Holcombe Boulevard, Houston, Texas, 77030, USA. Phone: 713.745.2803; Email: jabe@mdanderson.org (JA). Phone: 713.745.8262; Email: kfujiwara1@mdanderson.org (KF). Phone: 713.563.7433; Email: seevans@manderson.org (SEE). Or to: Nhat-Tu Le, Houston Methodist Research Institute, 6670 Bertner Avenue, R10-216 MS: R10 South, Houston, Texas 77930, USA. Phone: 713.363.8080; Email: Nhle@houstonmethodist.org.

JHW's present address is: Department of Obstetrics, Gynecology & Reproductive Sciences, The University of Texas Health Science Center at Houston, Houston, Texas, USA.

YF's present address is: Department of Radiology Research, Houston Methodist Research Institute, Houston, Texas, USA.

JHS's present address is: Department of Gastroenterology Hepatology & Nutrition, The University of Texas MD Anderson Cancer Center, Houston, Texas, USA.

1. Abe J, Berk BC. Novel mechanisms of endothelial mechanotransduction. *Arterioscler Thromb Vasc Biol.* 2014;34(11):2378–2386.
2. Le NT, Sandhu UG, Quintana-Quezada RA, Hoang NM, Fujiwara K, Abe JI. Flow signaling and atherosclerosis. *Cell Mol Life Sci.* 2017;74(10):1835–1858.
3. Camilleri M, et al. Pilot study of small bowel mucosal gene expression in patients with irritable bowel syndrome with diarrhea. *Am J Physiol Gastrointest Liver Physiol.* 2016;311(3):G365–G376.
4. Julià A, et al. A deletion at ADAMTS9-MAGI1 locus is associated with psoriatic arthritis risk. *Ann Rheum Dis.* 2015;74(10):1875–1881.
5. Alonso A, et al. Identification of risk loci for Crohn's disease phenotypes using a genome-wide association study. *Gastroenterology.* 2015;148(4):794–805.
6. Genetics of Personality Consortium, et al. Meta-analysis of genome-wide association studies for neuroticism, and the polygenic association with major depressive disorder. *JAMA Psychiatry.* 2015;72(7):642–650.
7. Laura RP, Ross S, Koeppen H, Lasky LA. MAGI-1: a widely expressed, alternatively spliced tight junction protein. *Exp Cell Res.* 2002;275(2):155–170.
8. Feng X, Jia S, Martin TA, Jiang WG. Regulation and involvement in cancer and pathological conditions of MAGI1, a tight junction protein. *Anticancer Res.* 2014;34(7):3251–3256.
9. Sakurai A, et al. MAGI-1 is required for Rap1 activation upon cell-cell contact and for enhancement of vascular endothelial cadherin-mediated cell adhesion. *Mol Biol Cell.* 2006;17(2):966–976.
10. Chastre E, et al. TRIP6, a novel molecular partner of the MAGI-1 scaffolding molecule, promotes invasiveness. *FASEB J.* 2009;23(3):916–928.
11. Blenis J. Signal transduction via the MAP kinases: proceed at your own RSK. *Proc Natl Acad Sci USA.* 1993;90(13):5889–5892.
12. Abe J, Okuda M, Huang Q, Yoshizumi M, Berk BC. Reactive oxygen species activate p90 ribosomal S6 kinase via Fyn and Ras. *J Biol Chem.* 2000;275(3):1739–1748.
13. Sakamoto KM, Frank DA. CREB in the pathophysiology of cancer: implications for targeting transcription factors for cancer therapy. *Clin Cancer Res.* 2009;15(8):2583–2587.
14. Frödin M, Gammeltoft S. Role and regulation of 90 kDa ribosomal S6 kinase (RSK) in signal transduction. *Mol Cell Endocrinol.* 1999;151(1-2):65–77.
15. Heo KS, Fujiwara K, Abe J. Disturbed-flow-mediated vascular reactive oxygen species induce endothelial dysfunction. *Circ J.* 2011;75(12):2722–2730.
16. Pearson G, English JM, White MA, Cobb MH. ERK5 and ERK2 cooperate to regulate NF-kappaB and cell transformation. *J Biol Chem.* 2001;276(11):7927–7931.
17. Le NT, et al. A crucial role for p90RSK-mediated reduction of ERK5 transcriptional activity in endothelial dysfunction and atherosclerosis. *Circulation.* 2013;127(4):486–499.
18. Heo KS, et al. Disturbed flow-activated p90RSK kinase accelerates atherosclerosis by inhibiting SENP2 function. *J Clin Invest.* 2015;125(3):1299–1310.
19. Heo KS, et al. De-SUMOylation enzyme of sentrin/SUMO-specific protease 2 regulates disturbed flow-induced SUMOylation of ERK5 and p53 that leads to endothelial dysfunction and atherosclerosis. *Circ Res.* 2013;112(6):911–923.
20. Heo KS, et al. PKC $\zeta$  mediates disturbed flow-induced endothelial apoptosis via p53 SUMOylation. *J Cell Biol.* 2011;193(5):867–884.
21. Traub O, Berk BC. Laminar shear stress: mechanisms by which endothelial cells transduce an atheroprotective force. *Arterioscler Thromb Vasc Biol.* 1998;18(5):677–685.

22. Heo KS, Berk BC, Abe J. Disturbed flow-induced endothelial proatherogenic signaling via regulating post-translational modifications and epigenetic events. *Antioxid Redox Signal*. 2016;25(7):435–450.
23. Thomas GM, Rumbaugh GR, Harrar DB, Haganir RL. Ribosomal S6 kinase 2 interacts with and phosphorylates PDZ domain-containing proteins and regulates AMPA receptor transmission. *Proc Natl Acad Sci USA*. 2005;102(42):15006–15011.
24. Xue Y, Ren J, Gao X, Jin C, Wen L, Yao X. GPS 2.0, a tool to predict kinase-specific phosphorylation sites in hierarchy. *Mol Cell Proteomics*. 2008;7(9):1598–1608.
25. Chang E, Abe J. Kinase-SUMO networks in diabetes-mediated cardiovascular disease. *Metab Clin Exp*. 2016;65(5):623–633.
26. Itahana Y, Yeh ET, Zhang Y. Nucleocytoplasmic shuttling modulates activity and ubiquitination-dependent turnover of SUMO-specific protease 2. *Mol Cell Biol*. 2006;26(12):4675–4689.
27. Heo KS, et al. Disturbed flow-activated p90RSK kinase accelerates atherosclerosis by inhibiting SENP2 function. *J Clin Invest*. 2015;125(3):1299–1310.
28. Ren J, et al. Systematic study of protein sumoylation: Development of a site-specific predictor of SUMOsp 2.0. *Proteomics*. 2009;9(12):3409–3412.
29. Dunn J, et al. Flow-dependent epigenetic DNA methylation regulates endothelial gene expression and atherosclerosis. *J Clin Invest*. 2014;124(7):3187–3199.
30. Nam D, et al. Partial carotid ligation is a model of acutely induced disturbed flow, leading to rapid endothelial dysfunction and atherosclerosis. *Am J Physiol Heart Circ Physiol*. 2009;297(4):H1535–H1543.
31. Merino H, Parthasarathy S, Singla DK. Partial ligation-induced carotid artery occlusion induces leukocyte recruitment and lipid accumulation—a shear stress model of atherosclerosis. *Mol Cell Biochem*. 2013;372(1-2):267–273.
32. Wang E, Albritton L, Ross SR. Identification of the segments of the mouse transferrin receptor 1 required for mouse mammary tumor virus infection. *J Biol Chem*. 2006;281(15):10243–10249.
33. Jung P, et al. Isolation and in vitro expansion of human colonic stem cells. *Nat Med*. 2011;17(10):1225–1227.
34. van der Flier LG, Haegerbarth A, Stange DE, van de Wetering M, Clevers H. OLFM4 is a robust marker for stem cells in human intestine and marks a subset of colorectal cancer cells. *Gastroenterology*. 2009;137(1):15–17.
35. Zeng L, et al. Sustained activation of XBP1 splicing leads to endothelial apoptosis and atherosclerosis development in response to disturbed flow. *Proc Natl Acad Sci USA*. 2009;106(20):8326–8331.
36. Todd DJ, Lee AH, Glimcher LH. The endoplasmic reticulum stress response in immunity and autoimmunity. *Nat Rev Immunol*. 2008;8(9):663–674.
37. Costa M, et al. Dynamic regulation of ERK2 nuclear translocation and mobility in living cells. *J Cell Sci*. 2006;119(Pt 23):4952–4963.
38. Adachi M, Fukuda M, Nishida E. Nuclear export of MAP kinase (ERK) involves a MAP kinase kinase (MEK)-dependent active transport mechanism. *J Cell Biol*. 2000;148(5):849–856.
39. Civelek M, Manduchi E, Riley RJ, Stoeckert CJ, Davies PF. Chronic endoplasmic reticulum stress activates unfolded protein response in arterial endothelium in regions of susceptibility to atherosclerosis. *Circ Res*. 2009;105(5):453–461.
40. Hirabayashi S, Tajima M, Yao I, Nishimura W, Mori H, Hata Y. JAM4, a junctional cell adhesion molecule interacting with a tight junction protein, MAGI-1. *Mol Cell Biol*. 2003;23(12):4267–4282.
41. Ichiki T, Izumi R, Cataliotti A, Larsen AM, Sandberg SM, Burnett JC. Endothelial permeability in vitro and in vivo: protective actions of ANP and omapatrilat in experimental atherosclerosis. *Peptides*. 2013;48:21–26.
42. Korshunov VA, Berk BC. Flow-induced vascular remodeling in the mouse: a model for carotid intima-media thickening. *Arterioscler Thromb Vasc Biol*. 2003;23(12):2185–2191.
43. Ko KA, et al. Developing a reliable mouse model for cancer therapy-induced cardiovascular toxicity in cancer patients and survivors. *Front Cardiovasc Med*. 2018;5:26.
44. Schneider CA, Rasband WS, Eliceiri KW. NIH Image to ImageJ: 25 years of image analysis. *Nat Methods*. 2012;9(7):671–675.
45. van Schadewijk A, van't Wout EF, Stolk J, Hiemstra PS. A quantitative method for detection of spliced X-box binding protein-1 (XBP1) mRNA as a measure of endoplasmic reticulum (ER) stress. *Cell Stress Chaperones*. 2012;17(2):275–279.
46. Hirota M, Kitagaki M, Itagaki H, Aiba S. Quantitative measurement of spliced XBP1 mRNA as an indicator of endoplasmic reticulum stress. *J Toxicol Sci*. 2006;31(2):149–156.
47. Rao X, Huang X, Zhou Z, Lin X. An improvement of the 2<sup>-</sup>(-delta delta CT) method for quantitative real-time polymerase chain reaction data analysis. *Biostat Bioinforma Biomath*. 2013;3(3):71–85.
48. Krämer A, Green J, Pollard J, Tugendreich S. Causal analysis approaches in Ingenuity Pathway Analysis. *Bioinformatics*. 2014;30(4):523–530.